# Formation of Minor Phases in a Nickel-Based Disk Superalloy

*T.P. Gabb*
*Glenn Research Center, Cleveland, Ohio*

*A. Garg*
*University of Toledo, Toledo, Ohio*

*D.R. Miller*
*The Ohio State University, Columbus, Ohio*

*C.K. Sudbrack, D.R. Hull, D. Johnson, R.B. Rogers, and J. Gayda*
*Glenn Research Center, Cleveland, Ohio*

*S.L. Semiatin*
*U.S. Air Force Research Laboratory, Wright-Patterson Air Force Base, Dayton, Ohio*

# NASA STI Program . . . in Profile

Since its founding, NASA has been dedicated to the advancement of aeronautics and space science. The NASA Scientific and Technical Information (STI) program plays a key part in helping NASA maintain this important role.

The NASA STI Program operates under the auspices of the Agency Chief Information Officer. It collects, organizes, provides for archiving, and disseminates NASA's STI. The NASA STI program provides access to the NASA Aeronautics and Space Database and its public interface, the NASA Technical Reports Server, thus providing one of the largest collections of aeronautical and space science STI in the world. Results are published in both non-NASA channels and by NASA in the NASA STI Report Series, which includes the following report types:

- TECHNICAL PUBLICATION. Reports of completed research or a major significant phase of research that present the results of NASA programs and include extensive data or theoretical analysis. Includes compilations of significant scientific and technical data and information deemed to be of continuing reference value. NASA counterpart of peer-reviewed formal professional papers but has less stringent limitations on manuscript length and extent of graphic presentations.

- TECHNICAL MEMORANDUM. Scientific and technical findings that are preliminary or of specialized interest, e.g., quick release reports, working papers, and bibliographies that contain minimal annotation. Does not contain extensive analysis.

- CONTRACTOR REPORT. Scientific and technical findings by NASA-sponsored contractors and grantees.

- CONFERENCE PUBLICATION. Collected papers from scientific and technical conferences, symposia, seminars, or other meetings sponsored or cosponsored by NASA.

- SPECIAL PUBLICATION. Scientific, technical, or historical information from NASA programs, projects, and missions, often concerned with subjects having substantial public interest.

- TECHNICAL TRANSLATION. English-language translations of foreign scientific and technical material pertinent to NASA's mission.

Specialized services also include creating custom thesauri, building customized databases, organizing and publishing research results.

For more information about the NASA STI program, see the following:

- Access the NASA STI program home page at *http://www.sti.nasa.gov*

- E-mail your question to *help@sti.nasa.gov*

- Fax your question to the NASA STI Information Desk at 443–757–5803

- Phone the NASA STI Information Desk at 443–757–5802

- Write to:
  STI Information Desk
  NASA Center for AeroSpace Information
  7115 Standard Drive
  Hanover, MD 21076–1320

# Formation of Minor Phases in a Nickel-Based Disk Superalloy

*T.P. Gabb*
*Glenn Research Center, Cleveland, Ohio*

*A. Garg*
*University of Toledo, Toledo, Ohio*

*D.R. Miller*
*The Ohio State University, Columbus, Ohio*

*C.K. Sudbrack, D.R. Hull, D. Johnson, R.B. Rogers, and J. Gayda*
*Glenn Research Center, Cleveland, Ohio*

*S.L. Semiatin*
*U.S. Air Force Research Laboratory, Wright-Patterson Air Force Base, Dayton, Ohio*

National Aeronautics and
Space Administration

Glenn Research Center
Cleveland, Ohio 44135

July 2012

# Acknowledgments

*Level of Review*: This material has been technically reviewed by technical management.

Available from

| | |
|---|---|
| NASA Center for Aerospace Information | National Technical Information Service |
| 7115 Standard Drive | 5301 Shawnee Road |
| Hanover, MD 21076–1320 | Alexandria, VA 22312 |

Available electronically at http://www.sti.nasa.gov

# Formation of Minor Phases in a
# Nickel-Based Disk Superalloy

T.P. Gabb
National Aeronautics and Space Administration
Glenn Research Center
Cleveland, Ohio 44135

A. Garg
University of Toledo
Toledo, Ohio 43606

D.R. Miller
The Ohio State University
Columbus, Ohio 43210

C.K. Sudbrack, D.R. Hull, D. Johnson, R.B. Rogers, and J. Gayda
National Aeronautics and Space Administration
Glenn Research Center
Cleveland, Ohio 44135

S.L. Semiatin
U.S. Air Force Research Laboratory
Wright-Patterson Air Force Base
Dayton, Ohio 45433

## Abstract

The minor phases of powder metallurgy disk superalloy LSHR were studied. Samples were consistently heat treated at three different temperatures for long times to approximate equilibrium. Additional heat treatments were also performed for shorter times, to then assess non-equilibrium conditions. Minor phases including MC carbides, $M_{23}C_6$ carbides, $M_3B_2$ borides, and sigma were identified. Their transformation temperatures, lattice parameters, compositions, average sizes and total area fractions were determined, and compared to estimates of an existing phase prediction software package. Parameters measured at equilibrium sometimes agreed reasonably well with software model estimates, with potential for further improvements. Results for shorter times representing non-equilibrium indicated significant potential for further extension of the software to such conditions, which are more commonly observed during heat treatments and service at high temperatures for disk applications.

## 1.0 Introduction

Structure, composition, contents and size distributions of carbide and boride phases can significantly influence the processing and mechanical properties of nickel-base superalloys (Refs. 1 to 6), especially at elevated temperatures where grain boundaries influence strength as well as time-dependent deformation and failure modes. Cubic MC carbides are stable up to very high temperatures near superalloy solidification, and therefore can help constrain grain growth during solution heat treatments above the gamma prime solvus (Ref. 7). The elements Ta, Ti, Nb, and W often combine with carbon to form this carbide. $M_{23}C_6$ carbides are stable at lower temperatures up to near 900 °C, and can improve the resistance to grain boundary sliding, rupture and dwell crack growth in service temperatures of 600 to 815 °C. Cr, Mo, and W can react with carbon to form this carbide. Boron in solid solution within the γ

matrix also improves the resistance to grain boundary sliding, rupture, and dwell crack growth (Ref. 5). Boride phase $M_3B_2$ has not been proven to specifically improve properties, but is often observed in disk superalloys containing boron. This phase can have a melting point only slightly higher than solution heat treatment temperatures (Ref. 6), to limit solution heat treatment upper tolerance temperatures. Mo, Cr, and W often combine with B to form this phase.

Harmful topological close packed (TCP) phases can also form in disk superalloys (Ref. 1 and 2). These phases such as σ, μ, Laves, and P have low inherent ductility due to limited slip systems, and can have needle or lathe morphologies, resulting in lower tensile and rupture ductilities at application temperatures (Refs. 8 and 9). Therefore, several models have been developed over the years to predict the formation of such phases (Refs. 10 and 11).

Recent advances in calculating thermodynamic properties of multi-component systems have enabled microstructural modeling software packages such as Thermo-Calc (Thermo-Calc Software, Inc.) (Ref. 12), JMatPro (Sente Software Ltd.) (Ref. 13), and Pandat (CompuTherm LLC) (Ref. 14) to estimate relative percentages and compositions of phases at equilibrium in superalloys at various temperatures. However, for use with a specific alloy of interest, this work has shown such estimates need to be compared with experimentally-measured phase identities and contents after known heat treatments approximating equilibrium, for model verification and potential refinements (Ref. 15). Experimental measurements at non-equilibrium conditions could also be used to help understand and model formation kinetics of minor phases. The primary objective of this work was to provide experimental composition, content, and size measurements of the predominant minor phases of the disk superalloy LSHR after varied heat treatments, for comparison with typical estimates of such software packages.

## 2.0    Materials and Procedures

Disk superalloy LSHR having a composition in weight percent of 3.46Al, 0.028B, 0.029C, 20.7Co, 12.52Cr, 0.07Fe, 2.73Mo, 1.45Nb, 1.6Ta, 3.50Ti, 4.33W, 0.049Zr, bal. Ni and trace impurities was produced through powder processing. It was atomized in argon, hot compacted, extruded and then isothermally forged into a flat, uniform disk 5.08 cm thick and 30.48 cm in diameter.

Phase extraction samples were removed by electro-discharge machining pins of about 10 g weight and 10 mm diameter in the circumferential direction from the rim of the disk. These samples were solution heat treated at 1199 °C for 1 h and furnace cooled at an average rate of 21 °C/min. They were then aged at 843 °C for 1,000 h and water quenched. Electrochemical extractions of minor phase were performed using a 10 ml HCl-1 g tartaric acid-90 ml methanol electrolyte. Triplicate extractions were performed in each case. Extracted phases and lattice parameters were identified using x-ray diffraction (XRD). XRD data was gathered with a Bruker D8 Advance (Bruker Corporation) diffractometer using Cu Kα radiation in a Bragg-Brentano geometry with a solid state linear position sensitive detector. Qualitative phase identification was performed using commercial software. Because of significant peaks overlapping, Rietveld refinement (Ref. 16) was then employed to determine lattice parameters using a fundamental parameters approach as implemented in the Bruker TOPAS (Bruker Corporation) software program. The Rietveld method employs (Ref. 17) a least-squares fitting approach using a mathematical model based on the scattered intensities of constituent crystalline phases. In the complex mixtures of phases examined in this work, the accuracy of the lattice parameters of any individual phase was limited by the amount of the phase present. The accuracy of major phases was estimated to be as high as 5 significant digits and that of trace phases was as low as 2 significant digits.

Small pins of 3 mm diameter and 16 mm long were also extracted in the circumferential direction near the rim of the disk, for various heat treatments. The conditions of these samples are summarized in Table 1. Samples were extracted from the extrusion before forging, and from the forging, for examination without further material processing. Single samples were only solution heat treated at 1199 °C for 1 h, then water quenched at an average cooling rate of 5,000 °C/min. or furnace cooled at a controlled average cooling rate of 21 °C/min. Additional samples were solution heat treated at 1199 °C for 1 h, water

quenched at an average cooling rate of about 5,000 °C/min to minimize phase nucleation and growth during the cooling process, and subsequently given aging heat treatments. They were aged at temperatures of 760, 843, and 927 °C for times of 10, 100, and 1,000 h and again water quenched, yielding nine different aged cases.

Differential thermal analysis (DTA) experiments were performed using a Netzsch STA 409C to help estimate the formation temperatures of minor phases, the solidus and the liquidus. Cylindral samples with 5 mm diameter and lengths ranging from 4 to 12 mm and weights from 683 to 1587 mg were extracted from the as-forged disk. The STA chamber was backfilled twice with Ar to remove oxygen before starting to heat. Under a 40 to 60 mL/min He flow, samples were heated quickly, either at 20 °C/min or at 10 °C/min, to a starting temperature, $T_{start}$, of 700 to 1000 °C. Then, using two rates, 5 and 2 °C/min, the samples were either i) heated and cooled three times between $T_{start}$ and a maximum temperature ($T_{max}$) of 1220 °C or ii) heated through melting to $T_{max}$ of 1342 to 1480 °C then cooled to $T_{start}$. Formation temperatures with distinct peaks, i.e. maximum $M_3B_2$ boride dissolution on heating, maximum $M_3B_2$ boride formation on cooling and the liquidus on heating, were determined from the intersections of tangential lines at the onset and at the tail of each transformation in the thermograms. Since the change in heat capacity at the solidus temperature is gradual, the solidus is difficult to determine from DTA measurements. Solidus was thus determined by inspecting in an enlarged view the intersection of the base line and the extrapolated tangent approximation of the thermogram. The temperature at which the MC carbides liquidate fully was estimated by the tangential intersections of the approximately flat slopes on either side of transition. To confirm this estimate, cylindrical samples with a 3 mm diameter and a 16 mm length were heat treated in air for 1 h at 1250, 1300, and 1325 °C, water quenched, metallographic prepared and examined using back-scattered SEM at 15 kV and energy dispersive X-ray spectrometry.

Selected heat treated and quenched samples were also sectioned and conventionally metallographically prepared. The sections were etched using a waterless Kallings etch. Linear intercept grain size was measured from optical images according to ASTM E112. Scanning electron microscope (SEM) evaluations were used to select samples for determination of minor phase compositions using TEM and microprobe. Thin disks of 3mm diameter and ~ 0.5mm thick were sliced and mechanically ground and polished from selected heat-treated samples. These disks were then electrochemically thinned to electron transparency using a solution of 10 percent perchloric and 90 percent methanol cooled to –30 °C. A FEI CM200 Transmission Electron Microscope (TEM) operating at 200 kV was used for imaging and to identify the crystal structure of predominant minor phases using selected area electron diffraction patterns (SAEDP) and energy dispersive X-ray spectrometry (EDS). Associated bright field images were used to estimate the typical size range and morphology of each phase. Sections having larger size minor phase particles were usually selected for estimation of minor phase compositions using a JEOL JXA-8200 scanning electron microprobe. At least 5 particles of each minor phase were analyzed.

Sizes and area fractions of various second phases were quantified via SEM using metallographically prepared sections, in order to sample sufficient areas. Samples were imaged in a Hitachi S-4700 Field Emission SEM at 20 kV using a working distance of 12 mm. Secondary electron and backscattered electron images were obtained at 2,000 x magnification, so that 4-8 grains and their associated boundaries would be captured within each image. This enabled statistically valid area fraction estimates to be determined for each phase in each image, even for phases such as $M_{23}C_6$ which was observed only at grain boundaries. Five adjacent images were acquired for each sample, with no bias of imaging towards a certain region of particles or grain boundaries. An EDAX CDU LEAP (EDAX, Inc.) detector attached to the SEM was used to obtain semi- quantitative chemical analysis of each particle visible in these images. Compositions determined from EDS spectra were then compared to results previously obtained in thin foil TEM evaluations. While the EDS spectra acquired using TEM and SEM were not identical, relative major elemental compositions for a given phase were consistent. Based on these analyses, the phase identity of each particle was recorded, and later used for size determinations of various phases. The combination of these techniques enabled discrimination and measurement of minor phase contents and particle sizes over a much larger imaged area than what would have been feasible using TEM alone.

Particle sizes were measured using Sigma Scan Pro 5.0 image analysis software. The difference in brightness between minor and γ-γ′ phases in secondary electron SEM images enabled brightness-based local thresholding. Each minor phase was measured separately, and also classified by location, either within grains or at grain boundaries. Area, equivalent radius, major axis, minor axis, and perimeter were determined for each particle. The equivalent radius calculation assumed a spherical shape and used the formula:

$$\text{Equivalent Radius} = \sqrt{\text{Area}/\pi}$$

Phase area fraction was determined by combining the areas of all particles of an identity and class within an image. Size-frequency histograms were generated for each phase with more than 10 particles acquired.

JMatPro-Ni6.0 and Pandat 8.1 software packages were used to predict minor phase characteristics, assuming thermodynamic equilibrium. However, only phases identified experimentally, using both powder X-ray diffraction of minor phase extractions and selected area electron diffraction patterns of particles within thin foils in the TEM, were selected in the phase catalogues for each package. The packages were otherwise used with no modifications or custom enhancements to the models or input databases, for these initial estimates.

# 3.0  Results and Discussion

## 3.1  Heat Treatments

Typical SEM images of samples after extrusion and after subsequent forging are compared in Figure 1. Linear intercept grain sizes of these samples were 4.1 and 5.5 µm, respectively. The large dark phase particles are primary γ′, with mean radius of 0.4 and 1.1 µm, respectively. These particles acted to constrain grain growth during extrusion and forging. Samples subsequently solution heat treated at 1199 °C for 1 h and either furnace cooled or water quenched are compared in Figure 2. The primary γ′ particles have dissolved during this solution treatment. Supersolvus solution heat treatments thereby allowed grain growth to a larger linear intercept grain size, near 25 µm. Only MC carbides and $M_3B_2$ borides were identified at significant quantities in these samples. Images of samples aged 1,000 h to approach equilibrium at 760, 843, and 927 °C are compared in Figure 3. MC and $M_{23}C_6$ carbides, $M_3B_2$ borides, and σ phase were identified in these conditions. Images of samples aged for shorter times, 10 and near 100 h, are also compared for 760, 843, and 927 °C in Figure 4, 5, and 6, respectively. The formation and growth of some of these phases with increasing aging time are evident.

Figure 7 shows thermograms from the DTA experiments. SEM imaging of forged samples that were heat treated in air for 1 h at 1250, 1300, and 1325 °C and then water quenched are compared in Figure 8. These heat treatment temperatures are all above the average DTA solidus value of 1239.5 °C, which was near the respective JMatPro and Pandat predictions of 1234.8 and 1260.5 °C, Table 2. This SEM evaluation established that the DTA solidus is reasonable. It is clear that some of grain boundaries have melted during the 1250 °C heat treat and then resolidified upon quenching. With increasing temperature, more of this melting and resolidification was observed. Mean liquidus measured with an average of four DTA runs was 1334.1 ± 2.3 °C, near the JMatPro prediction of 1340 °C and significantly below that of Pandat, 1402.8 °C.

## 3.2  Minor Phases

Predominant phases detected by x-ray diffaction and TEM observations are identified with measured lattice parameters in Table 3. MC and $M_{23}C_6$ carbides, $M_3B_2$ boride, and σ phases were identified by these approaches, and are shown in Figure 9 to 12. Compositions measured in atomic percent are compared to those predicted by JMatPro and Pandat in Table 4.

Subsequent measurements of minor phases over multiple SEM images indicated the equivalent radius of each minor phase could be assumed normally distributed (Figs. 13 to 16), so that the size distribution could be approximated using mean and standard deviation for each phase. Resulting SEM measurements of equivalent radius and area fraction for MC and $M_{23}C_6$ carbides are compared in Tables 5 and 6. Equivalent radius and area fraction results for $M_3B_2$ boride and σ phase particles are compared in Tables 7 and 8. Total area fractions of these minor phases measured after aging for 1,000 h are compared to those predicted by JMatPro and Pandat in Table 9.

## 3.3  MC Carbides

Figure 9 shows a typical TEM image and diffraction pattern of MC carbides. These carbides have an FCC Fm3m crystal structure, with a lattice parameter of a = 4.3820 angstroms (Å). This was comparable to that reported for several other disk superalloys (Ref. 18), but slightly higher than that reported for Rene 88DT, an alloy somewhat similar in composition to LSHR (Ref. 19). Typical size-frequency histograms acquired for MC carbides are shown in Figure 13. Equivalent radius and area fraction are tabulated versus sample condition in Table 5. MC carbide average equivalent radius did not excede 0.27 μm, making quantitative microprobe measurements of the composition difficult. EDS measurements of these carbides in TEM thin foils indicated this phase had an approximate composition of 12Nb-12Ta-26Ti-50C in atomic percent, Table 4. Quantitative compositions are not often reported for minor phases such as carbides and borides existing at such small sizes, due to difficulties of in-situ measurements using scanning electron microscopy. However, surveys indicate many other disk superalloys also have MC carbides which contain Ti, Ta, and Nb (Refs. 1, 2, 18, and 19). The slightly higher lattice parameter compared to Rene 88DT could be related to the presence of Ta in MC carbides for LSHR. The measured composition was near that predicted at equilibrium by Pandat, but markedly differed in Ti and Zr contents from JMatPro estimates. Overall MC carbide size, morphology, and area fraction appeared comparable in most samples, indicating high overall phase stability for the various conditions examined. While most appeared spherical or slightly elliptical in the SEM images presented, TEM examinations indicated the MC carbides usually had short cylindrical or blocky shapes, each made up of a single crystal.

Yet, some changes in MC carbides were observed when comparing those within grains versus at grain boundaries. Over 80 percent of the carbides were observed at grain boundaries for the as-extruded condition, Figure 1(a). About 35 percent of the carbides were observed at grain boundaries after forging, Figure 1(b). However, no more than 23 percent were observed at grain boundaries for samples supersolvus heat treated and subsequently furnace cooled or water quenched and aged, Figure 2 to 6. Here they more often appeared within the grains, sometimes loosely distributed in clusters. Therefore, a majority of these carbides did not appear to pin grain boundaries, to ultimately constrain grain growth during these solution heat treatments. The MC carbides at grain boundaries were often slightly larger than those within grains. This suggested that larger MC carbides may be more effective at pinning grain boundaries. MC carbide content at grain boundaries decreased with increasing aging time at 843 °C, which will be further considered below.

Overall MC carbide content was estimated at equilibrium conditions using JMatPro and Pandat in Table 9. The estimates agree reasonably well with experimental measurements at 927 and 843 °C, Figure 17, and suggest that MC carbides remained near equilibrium for samples aged at these temperatures for 1,000 h up to 1200 °C. A much lower content was estimated by JMatPro and Pandat at 760 °C, not observed in the experimental measurements. However, MC carbide content at grain boundaries was observed to decrease with increasing aging time at 843 °C (Table 5), which will be further considered below.

The average measured MC phase transformation temperature of 1310.2 °C agreed reasonably well with that predicted by JMatPro and Pandat, 1303.1 and 1316.7 °C respectively, as indicated in Table 2. The 1300 and 1325 °C heat treatments are lower and upper bounds for the DTA extracted temperature for full liquation of the MC carbides at 1310 °C; however locating MC carbides to image and analyze with

EDS was challenging for these conditions. The MC carbides that were located in the three samples quenched from the high temperature are compared in Figure 8.

## 3.4    $M_{23}C_6$ Carbides

Figure 10 shows a typical TEM image and diffraction pattern of $M_{23}C_6$ carbides. These carbides have an FCC Fm3m crystal structure, with lattice parameter estimated using TEM of 10.6 Å. This is very close to that reported for Rene 88DT (Ref. 19). The average phase composition was measured by microprobe on a sample aged 843 °C/1,000 h, having particles sometimes as large as 0.5μm radius, as shown in Figure 5. Microprobe quantitative measurements indicated this phase had an approximate composition of 20.6Co-33.0Cr-5.4Mo-14.3Ni-5-2.5W-24.2C in atomic percent, Table 4. Surveys indicate other disk superalloys also have $M_{23}C_6$ carbides which are principally high in Cr and Mo (Refs. 1, 2, 18, and 19). The high Co and Ni content measured here implies these elements can substitute for Cr in LSHR. Measured composition significantly differed from JMatPro and Pandat equilibrium predictions in Cr content. Co can apparently substitute for Cr in $M_{23}C_6$ far more than predicted at equilibrium by JMatPro and Pandat. The $M_{23}C_6$ carbides populated this alloy as particles often elongated along the grain boundaries. However, larger particles sometimes resided at triple points. This gave a skewed size-frequency distribution, as shown by the size-frequency histograms in Figure 14. TEM evaluations indicated the elongated particles were often made up of multiple grains. These carbides were not found away from grain boundaries. While some of these particles were highly elongated, equivalent radius was calculated to enable consistent comparisons among all particles and minor phases in this study.

Mean equivalent radius and area fraction of $M_{23}C_6$ carbides are tabulated versus sample condition in Table 6. These carbides were not found in any samples that were not given aging heat treatments. This indicates that significant time is required at the aging temperatures for carbide formation to occur, exclusively at grain boundaries. Results in Table 6 show consistent trends in growth and dissolution for the different times and temperatures investigated. At both 760 and 843 °C, the average equivalent radius and area fraction increased with time. This trend was enhanced at 843 °C, where the longest aging time of 1,000 h produced the highest phase area fraction of 0.0042 and equivalent mean radius near 0.29 μm for this phase. Significant growth occurred at this temperature, where number density decreased while particle radius increased. Recall from Table 5 that MC carbide content at grain boundaries decreased with increasing time at 843 °C. No evidence of MC carbides being partially transformed to $M_{23}C_6$ carbides was directly observed for these samples, as previously reported for several other nickel-base superalloys (Refs. 1 and 2). Due to the difficulties in isolating such particles in SEM and TEM, this transformation could still exist. However, based on the much wider spacing of prior MC carbides compared to that of $M_{23}C_6$, it appears that nucleation and growth of new particles accounted for a large majority of the $M_{23}C_6$ phase particles observed in aged specimens. No $M_{23}C_6$ carbides were observed within grains in any of the aged conditions, however many MC carbides could be found. At 927 °C, $M_{23}C_6$ formed after 10 h aging, but not at longer times, indicating it is not stable at this temperature. Thus as the aging time increased and conditions approached equilibrium, the size and area fraction were driven to zero.

Total $M_{23}C_6$ carbide content is compared to that estimated at equilibrium conditions using JMatPro and Pandat in Table 9 and Figure 17. The estimates agree fairly well with experimental measurements, but suggest that $M_{23}C_6$ carbide contents were still approaching equilibrium even for samples aged 1,000 h. The models predicted equilibrium of $M_{23}C_6$ carbides and elimination of MC carbides at temperatures of 760 to near 900 °C. However, this transformation appears to be very slow at these temperatures, and there was no evidence observed supporting this transformation for MC carbide particles away from grain boundaries.

$M_{23}C_6$ carbide formation temperature was predicted to be 851 and 987.9 °C using JMatPro and Pandat; however, no change in the thermograms was detected between 800 to 1000 °C during heating at 5, 10, and 20 °C/min, due to the lack of detectable $M_{23}C_6$ carbides in the tested as-forged samples.

### 3.5    M₃B₂ Borides

Figure 11 shows the a typical TEM image and diffraction pattern of $M_3B_2$ borides. These borides have a tetragonal P4/mbm crystal structure, with lattice parameters estimated as a = 5.791 Å, b = 3.11 Å. These lattice parameters are comparable to those reported for other disk alloys (Refs. 18, and 19). EDS and microprobe measurements on a sample aged 927 °C for 1,000 h indicated this phase had an approximate composition of 3.2Co-18.8Cr-15.8Mo-2.4Nb-4.5Ni-0.7Ta-2.4Ti-8.7W-3.8C-39.7B in atomic percent, Table 4. Surveys in the literature have also reported $M_3B_2$ borides rich in Cr, Mo and W (Refs. 1, 2, 18, and 19). The measurements indicate W can substitute for Mo significantly more than predicted at equilibrium by JMatPro and Pandat. Typical size-frequency histograms acquired for $M_3B_2$ borides are shown in Figure 15. Mean equivalent radius and area fraction are tabulated versus sample condition in Table 7 for $M_3B_2$ borides. These borides were most numerous in the as-extruded sample, as fine particles less than 0.4 μm radius chiefly along the grain boundaries. The quantity observed along grain boundaries was greatly reduced by forging. Most borides dissolved after the supersolvus solution heat treatment, but widely scattered borides less than 0.5 μm radius reappeared both within grains and at grain boundaries for long aging times at 760 and 843 °C. The highest area fraction for each temperature was found at the longest aging time of 1,000 h. The overall highest area fraction and average size of these borides was observed for 1,000 h aging at 927 °C, where they grew into the largest minor phase particles found in this study, of 1.19 μm radius.

Overall $M_3B_2$ boride content is estimated at equilibrium conditions using JMatPro and Pandat in Table 9. This was estimated to be essentially constant from 760 to 927 °C. The estimates were nearest experimental measurements at 927 °C, where measured content exceeded predictions. However at lower temperatures of 760 and 843 °C, $M_3B_2$ boride content was far below equilibrium estimates. This may be related in part to differences in equilibrium composition predicted versus that measured.

The average dissolution temperature on initial heating was estimated by DTA to be 1206.7 °C for heating at 5 °C/min, and 1202.8 °C for heating at 2 °C/min. The first cycle in the heating thermogram shows a slightly higher temperature for the maximum rate of $M_3B_2$ liquation than subsequent cycles (Fig. 7, Table 2). This is believed to be a result of a microstructural change in state associated with cycling. As is typical for DTA measurements, heavier samples and samples heated at faster rates show temperatures slightly above, within 3.6 °C here, than lighter, more slowly heated samples. Melting leads to an increase of 3 to 8 °C in the maximum rate of $M_3B_2$ formation observed during cooling. Overall mean $M_3B_2$ liquation measured with an average of three single cycle DTA runs was 1201.3 ± 0.4 °C. Mean $M_3B_2$ formation temperature during cooling was measured to be 1179.2 °C, which is significantly lower than respective JMatPro and Pandat equilibrium predictions of 1243.8 and 1269.0 °C. This also may be related in part to differences in equilibrium compositions predicted versus those measured. But boride formation was apparently very slow for these lower temperature conditions.

### 3.6    σ

Figure 12 shows a TEM image and diffraction pattern of σ phase particles. This phase had a tetragonal P42/mnm crystal structure, with lattice parameters a = 8.888 Å, c = 4.593 Å. These lattice parameter measurements are about 3.5 percent smaller than those made on σ phase particles in N18 (Ref. 20). Observed σ precipitates were too small for composition measurements using the microprobe. Particles were separated by electrochemical phase extraction, and then analyzed by EDS in the SEM. This required careful backscatter electron imaging to locate small acicular σ particles that were isolated away from more cuboidal MC and spherical $M_3B_2$ particles. Their composition was found to be 27.6Co-26.1Cr-14.2Mo-11.7Ni-4.1Ta-2.4Ti-14.0W in atomic percent, Table 4. The current measurements differ significantly from that measured in prior work for many superalloys having different overall compositions than LSHR (Refs. 1, 2, 8, and 9). Yet, roughly similar Co, Ni, and Mo contents were measured in the σ phase particles analyzed in N18 (Ref. 20), although at a higher Cr level. The measured composition also

differed from that estimated at equilibrium using JMatPro and Pandat, which predicted higher Cr, lower W, and no Ta or Ti.

Typical size-frequency histograms acquired for these σ phase particles are shown in Figure 16. Mean equivalent radius and area fraction are tabulated versus sample condition in Table 8. σ phase particles were found in a minority of examined cases, attaining a maximum area fraction of 0.00327 at 843 °C for 1,000 h. They appeared as irregular shapes at the grain boundaries, and seemed more elongated when nucleated in the grains. Some had distinct needle-like shapes. Several σ phase particles were also found to be attached to small MC carbides. These σ particles sometime appeared to have nucleated on the MC carbides, as this could require less energy. Figure 18 depicts two examples of this, observed in thin foils using TEM. During aging at 843 and 927 °C, the σ particles appeared to precipitate first at the triple points of grain boundaries, and later within the grains. However, they were not observed after 1,000 h at 927 °C, indicating they were not stable at this temperature.

Total σ content is estimated at equilibrium conditions using JMatPro and Pandat in Table 9. The estimates are significantly greater than experimental measurements. This may be largely related to the differences in composition predicted at equilibrium versus that measured. But the test data indicates that σ phase content was only slowly increasing and at very low levels, and did not reach equilibrium for these heat treatment conditions. Yet, formation of the very small quantities of σ as observed here appears possible for extended service times near 843 °C.

σ phase formation temperature was predicted to be 865 and 1016 °C using JMatPro and Pandat ; however, no change in the thermograms was detected between 800 to 1000 °C during heating at 5, 10, and 20 °C/min, due to the lack of detectable σ phase in the tested as-forged samples.

### 3.6.1 Potential Future Work

Additional techniques to further verify the compositions of these minor phases as functions of heat treatment are necessary. Significant differences in phase compositions exist between current experimental measurements, findings for prior generation superalloys, and equilibrium model predictions. Errors in assumed phase compositions could significantly influence many model predictions based on mass conservation, thermodynamics, and kinetic properties. Additional aging heat treatments after slower, more varied cooling paths other than the water quench treatment employed here would also be useful, to understand cooling path dependencies on composition, precipitation, and coarsening of minor phases during quench and subsequent aging heat treatments. Similar aging heat treatments on other disk alloys could then allow understanding of alloy composition effects on minor phase precipitation.

## 4.0 Conclusions

Carbide and boride phase contents and sizes can vary significantly with heat treatment temperature and time, and at short times significantly diverge from equilibrium conditions. Commercial software such as JMatPro and Pandat can provide estimates of equilibrium contents of MC, $M_{23}C_6$ carbides, $M_3B_2$ and σ phases, representing upper limits for samples aged for a long time to simulate equilibrium conditions. The predictions were closest at 927 °C, where equilibrium conditions were most nearly attained. Longer times than 1,000 h appear necessary to approach equilibrium at lower temperatures of 843 and 760 °C, where predicted $M_3B_2$ and σ contents greatly exceeded measurements. Yet, the applied aging times are relevant, as they do encompass disk heat treatment times and accumulated service time at high temperatures. The predictions of phase formation temperatures reported here appear to be useful for initial estimates, although $M_3B_2$ predictions can be improved. The errors in predictions may be primarily related to divergences in predicted phase compositions from experimental measurements. In addition, the partially predicted total replacement of MC with $M_{23}C_6$ carbides at these lower temperatures appears to only be occurring at grain boundaries, which would ultimately exert lower limits to MC carbide content and upper limits to $M_{23}C_6$ carbide contents at equilibrium. Enhanced prediction software would be necessary to fully simulate these factors, and to predict phase contents and sizes at shorter aging times of 1 to 10 h, as

typically used in aging heat treatments. As maximum disk application temperatures rise, accurate simulation of these factors could become important for both processing and service life design.

## References

1. C. T. Sims, N. S. Stoloff, W. C. Hagel, Superalloys II, John Wiley & Sons, Inc., New York, 1987, pp. 91-133.
2. R. C. Reed, The Superalloys, Cambridge University Press, 2006, pp. 35-54.
3. R. F. Decker, "Strengthening Mechanismss in Nickel-Base Superalloys," Steel Strengthening Mechanisms Symposium, Climax Molybdenum Company, 1969.
4. S. Floreen, J. M. Davidson, "The Effects of B and Zr on the Creep and Fatigue Crack Growth Behavior of a Ni-base Superalloy," Met Trans. A, V. 14A, 1983, pp. 895-901.
5. T. J. Garosshen, T. D. Tillman, G. P. McCarthy, "Effects of B, C, and Zr on the Structure and Properties of a P/M Nickel Base Superalloy," Met. Trans. A, V. 18A, 1987, pp. 69-77.
6. E. S. Huron, K. R. Bain, D. P. Mourer, J. J. Schirra, P. L. Reynolds, E. E. Montero, "The Influence of Grain Boundary Elements on Properties and Microstructures of P/M Nickel Base Superalloys," Superalloys 2004, ed. K. A. Green, T. M. Polock, H. Harada, T. E. Howson, R. C. Reed, J. J. Schirra, S. Walston, TMS, Warrendale, PA, 2004, pp. 73-81.
7. E. L. Raymond, R. D. Kissinger, A. J. Paxson, E. S. Huron, "Method for Forming a Nickel-base Superalloy Having Improved Resistance to Abnormal Grain Growth," U.S. Patent 5,584,947, U.S. Patent Office, 1996.
8. R. L. Dreshfield, R. Ashbrook, "Sigma Phase Formation and Its Effect on Stress Rupture Properties of IN-100," NASA TND-5185, Washington, D.C., April 1965.
9. R. C. Reed, M. P. Jackson, Y. S. Na, "Characterization and Modeling of the Precipitation of the Sigma Phase in Udimet 720 and Udimet 720LI," Met. Trans. A, V. 30A, 1999, pp. 521-533.
10. H. Murphy, C. T. Sims, "Phacomp Revisited," Symp. On Structural Stability in Superalloys, ASTM-ASME, 1968, pp. 47-66.
11. M. Moringa, N. Yukawa, H. Ezaki, H. Adachi, "New PHACOMP and Its Applications to Alloy Design (Phase Computation)," Superalloys 1984, ed. M. Gell, C. S. Kortovich, R. H. Bricknell, W. B. Kent, J. F. Radavich, The Metallurgical Society of AIME, 1984, pp. 523-532.
12. N. Saunders, "Phase Diagram Calculations for Ni-Based Superalloys," Superalloys 1996, ed. R. D. Kissinger, D. J. Deye, D. L. Anton, A. D. Cetel, M. V. Nathal, T. M. Pollock, D. A. Woodford, The Minerals, Metals, and Materials Society, Warrendale, PA, 1996, pp. 101-110.
13. N. Saunders, Z. Guo, X. Li, A. P. Miodownik, J.-P. Schille, "Modelling The Material Properties and Behavior of Ni-Based Superalloys," Superalloys 2004, ed. K.A. Green, T.M. Pollock, H. Harada, T.E. Howson, R.C. Reed, J.J. Schirra, and S. Walston. The Minerals, Metals, and Materials Society, Warrendale, PA, 2004, pp. 849-858.
14. W. Cao, S.-L. Chen, F. Zhang, K. Wu, Y. Yang, Y. A. Chang, R. Schmid-Fetzer, W. A. Oates, "PANDAT Software with PanEngine, PanOptimizer and PanPrecipitation for Multi-Component Phase Diagram Calculation and Materials Property Simulation," Calphad, V. 33(2), 2009, pp. 328-342.
15. J.-C. Zhao, M. F. Henry, "The Thermodynamic Prediction of Phase Stability in Multicomponent Superalloys," Journal of Metals, V. 54 (1), 2002, pp. 37-41.
16. H.M. Rietveld, "A Profile Refinement Method for Nuclear and Magnetic Structures," J. Appl. Crystallography, V. 2, 1969, pp. 65-71.
17. 17. R.W. Cheary and A.A. Coleho, "A Fundamental Parameters Approach of X-ray Line-profile Fitting," J. Appl. Crystallography, V. 25, 1992, pp. 109-121.
18. T. P. Gabb, A. Garg, D. L. Ellis, "Microstructural Evaluations of Baseline HSR/EPM Disk Alloys," NASA/TM-2004-213123, Washington, D.C., 2004.

19. S. T. Wlodek, M. Kelly, D. A. Alden, "The Structure of Rene′ 88DT," Superalloys 1996, ed. R. D. Kissinger, D. J. Deye, D. L. Anton, A. D. Cetel, M. V. Nathal, T. M. Pollock, D. A. Woodford, TMS, Warrendale, PA, 1996, pp. 129-136.
20. S. T. Wlodek, M. Kelly, D. A. Alden, "The Structure of N18," Superalloys 1992, ed. S. D. Antolovich, R. W. Stusrud, R. A. MacKay, D. L. Anton, T. Khan, D. L. Klarstrom, TMS, Warrendale, PA, 1992, pp. 467-476.

TABLE 1.—CONDITIONS OF LSHR SAMPLES ANALYZED

| Sample ID | Solution temperature, °C | Solution temperature, °C | Solution Quench | Aging temperature, °C | Aging temperature, °C | Aging quench |
|---|---|---|---|---|---|---|
| LAE-As-extruded | | | | | | |
| LAF-Extruded+Forged | | | | | | |
| LFF | 1199 | 1 | Furnace | | | |
| LFW | 1199 | 1 | Water | | | |
| LFW760-10 | 1199 | 1 | Water | 760 | 10 | Water |
| LFW760-100 | 1199 | 1 | Water | 760 | 100 | Water |
| LFW760-1k | 1199 | 1 | Water | 760 | 1000 | Water |
| LFW843-10 | 1199 | 1 | Water | 843 | 10 | Water |
| LFW843-100 | 1199 | 1 | Water | 843 | 100 | Water |
| LFW843-1k | 1199 | 1 | Water | 843 | 1000 | Water |
| LFW927-10 | 1199 | 1 | Water | 927 | 10 | Water |
| LFW927-99 | 1199 | 1 | Water | 927 | 99 | Water |
| LFW927-1k | 1199 | 1 | Water | 927 | 1000 | Water |

TABLE 2.—MEASURED TRANSFORMATION TEMPERATURES USING DIFFERENTIAL THERMAL ANALYSIS FOR AS-FORGED LSHR SAMPLES, COMPARED TO THOSE PREDICTED BY JMATPRO-NI 6.0 AND PANDAT 8.1

| Temperature rate, initial weight | $T_{start}$ °C | $T_{max}$ °C | Cycle | $M_3B_2$ liquation (heating) | $M_3B_2$ formation (cooling) | Solidus (heating) | MC liquation (heating) | Liquidus (heating) |
|---|---|---|---|---|---|---|---|---|
| 5 °C/min 1586.5 mg | 1000 | 1220 | First | 1207.6 | 1175.2 | ------- | ------- | ------- |
| | | | Second | 1201.3 | 1173.1 | ------- | ------- | ------- |
| | | | Third | 1202.4 | 1174.8 | ------- | ------- | ------- |
| 683.1 mg | 700 | 1370 | Single | 1205.8 | 1183.2 | 1240 | 1310.5 | 1334.5 |
| 2 °C/min 1.5012 mg | 1000 | 1220 | First | 1204.0 | 1179.6 | ------- | ------- | ------- |
| | | | Second | 1200.5 | 1177.6 | ------- | ------- | ------- |
| | | | Third | 1201.0 | 1177.6 | ------- | ------- | ------- |
| 915.6 mg | 850 | 1342 | Single | 1202.8 | 1185.6 | 1239 | 1310 | 1330.8 |
| 816.2 mg | 1000 | 1475 | Single | 1202.0 | 1181.9 | 1240 | 1310 | 1336.1 |
| 854.4 mg | 1000 | 1480 | Single | 1202.1 | 1183.5 | 1239 | ND | 1335.0 |
| | | | JMatPro | | 1243.8 | 1234.8 | 1303.1 | 1340.0 |
| | | | Pandat | | 1269.0 | 1260.5 | 1316.7 | 1402.8 |

TABLE 3.—PHASE LATTICE PARAMETERS ESTIMATED BY TEM SELECTED
AREA ELECTRON DIFFRACTION PATTERNS (SAEDP) OF THIN FOILS,
AND BY X-RAY DIFFRACTION OF MINOR PHASE EXTRACTIONS

| Phase | Structure | | | TEM | X-ray |
|---|---|---|---|---|---|
| MC | FCC, Fm3m | | a (Å) | 4.3 | 4.3820±0.0003 |
| $M_{23}C_6$ | FCC, Fm3m | | a (Å) | 10.6 | ------------------ |
| σ | Tetragonal, P4/mbm | | a (Å) | 8.9 | 8.888±0.001 |
| | | | c (Å) | 4.6 | 4.593±0.001 |
| $M_3B_2$ | Tetragonal, P42/mnm | | a (Å) | 6.0 | 5.791±0.008 |
| | | | c (Å) | 3.15 | 3.11±0.01 |

TABLE 4.—MEASURED COMPOSITIONS OF MINOR PHASES IN ATOMIC PERCENT,
COMPARED TO THOSE PREDICTED BY JMATPRO-NI 6.0 AND PANDAT 8.1

| Phase | Condition | Atomic % | Al | Co | Cr | Mo | Nb | Ni | Ta | Ti | W | C | B | Zr |
|---|---|---|---|---|---|---|---|---|---|---|---|---|---|---|
| MC | LFW760-1k | Mean | | | | | 12 | | 12 | 26 | | 50 | | |
| | | StanDev | | | | | 1.4 | | 1.5 | 1.6 | | | | |
| | | JMatPro (760 °C) | | | | | 10 | | 9.1 | 0.6 | 0.1 | 49.5 | | 30.7 |
| | | Pandat (978°C) | | | 4.7 | 1.3 | 8.9 | | 8 | 22.3 | 0.5 | 47.1 | | 7.3 |
| $M_{23}C_6$ | LFW843-1k | Mean | | 20.6 | 33.0 | 5.4 | | 14.3 | | | 2.5 | 24.2 | | |
| | | StanDev | | 1.6 | 3.8 | 0.6 | | 3.7 | | | 0.2 | 6.1 | | |
| | | JMatPro (760 °C) | | 5.6 | 59.7 | 9.5 | | 4.0 | | | 0.4 | 20.7 | | |
| | | Pandat (760 °C) | | 5.6 | 70.3 | 1.9 | | 1.1 | | | 0.4 | 20.7 | | |
| $M_3B_2$ | LFW927-1k | Mean | | 3.2 | 18.8 | 15.8 | 2.4 | 4.5 | 0.7 | 2.4 | 8.7 | 3.8 | 39.7 | |
| | | StanDev | | 0.4 | 1.6 | 1.7 | 0.4 | 0.1 | 0.1 | 0.2 | 1.0 | 1.3 | 5.8 | |
| | | JMatPro (927 °C) | | 0.4 | 20.7 | 37.6 | | 0.2 | | | 1.1 | | 40.0 | |
| | | Pandat (927 °C) | | 1.7 | 19.9 | 36.6 | | 0.7 | | | 1.1 | | 40.0 | |
| Sigma | LFW843C-1k | Mean | | 27.6 | 26.1 | 14.2 | | 11.7 | 4.1 | 2.4 | 14.0 | | | |
| | | StanDev | | 1.7 | 1.6 | 1.5 | | 0.6 | 1.4 | 0.7 | 1.5 | | | |
| | | JMatPro (843 °C) | | 28.8 | 47.7 | 10.2 | | 11.5 | | | 1.7 | | | |
| | | Pandat (843 °C) | | 31.0 | 42.5 | 8.7 | | 7.0 | | | 10.8 | | | |

TABLE 5.—EQUIVALENT RADIUS AND AREA FRACTION OF MC CARBIDES WITHIN GRAINS (WG)
AND AT GRAIN BOUNDARIES (GB), SAMPLE CONDITIONS DESCRIBED IN TABLE 1

| Sample | MC: WG average radius, μm | WG StDev radius, μm | Count, n | WG average area fraction | WG StDev area fraction | GB average radius, μm | GB StDev radius, μm | Count, n | GB average area fraction | GB StDev area fraction | Sum WG+GB area fraction |
|---|---|---|---|---|---|---|---|---|---|---|---|
| LAE-As extruded | 0.139 | 0.057 | 24 | 0.00012 | 0.00009 | 0.137 | 0.048 | 145 | 0.00068 | 0.00013 | 0.00080 |
| LAF-As forged | 0.151 | 0.043 | 110 | 0.00060 | 0.00012 | 0.164 | 0.055 | 60 | 0.00040 | 0.00010 | 0.00100 |
| LFF | 0.179 | 0.065 | 199 | 0.00160 | 0.00021 | 0.248 | 0.087 | 23 | 0.00035 | 0.00027 | 0.00195 |
| LFW | 0.174 | 0.062 | 193 | 0.00150 | 0.00069 | 0.163 | 0.067 | 20 | 0.00014 | 0.00008 | 0.00164 |
| LFW760-10 | 0.161 | 0.052 | 219 | 0.00139 | 0.00006 | 0.177 | 0.052 | 29 | 0.00022 | 0.00005 | 0.00161 |
| LFW760-100 | 0.171 | 0.059 | 236 | 0.00172 | 0.00040 | 0.195 | 0.066 | 18 | 0.00017 | 0.00017 | 0.00189 |
| LFW760-1k | 0.175 | 0.058 | 247 | 0.00187 | 0.00039 | 0.223 | 0.079 | 24 | 0.00030 | 0.00016 | 0.00217 |
| LFW843-10 | 0.189 | 0.061 | 237 | 0.00207 | 0.00018 | 0.222 | 0.062 | 44 | 0.00052 | 0.00007 | 0.00259 |
| LFW843-100 | 0.195 | 0.052 | 211 | 0.00191 | 0.00039 | 0.223 | 0.078 | 23 | 0.00028 | 0.00006 | 0.00219 |
| LFW843-1k | 0.191 | 0.069 | 184 | 0.00169 | 0.00041 | 0.262 | 0.079 | 9 | 0.00015 | 0.00014 | 0.00184 |
| LFW927-10 | 0.192 | 0.051 | 164 | 0.00143 | 0.00029 | 0.207 | 0.080 | 49 | 0.00054 | 0.00071 | 0.00197 |
| LFW927-99 | 0.177 | 0.055 | 129 | 0.00099 | 0.00031 | 0.268 | 0.102 | 15 | 0.00027 | 0.00023 | 0.00126 |
| LFW927-1k | 0.192 | 0.072 | 265 | 0.00248 | 0.00111 | 0.239 | 0.094 | 36 | 0.00053 | 0.00030 | 0.00301 |

TABLE 6.—EQUIVALENT RADIUS AND AREA FRACTION OF $M_{23}C_6$ CARBIDES WITHIN GRAINS (WG)
AND AT GRAIN BOUNDARIES (GB), SAMPLE CONDITIONS DESCRIBED IN TABLE 1

| Sample | $M_{23}C_6$: WG average radius, μm | WG StDev radius, μm | Count, n | WG average area fraction | WG StDev area fraction | GB average radius, μm | GB StDev radius, μm | Count, n | GB average area fraction | GB StDev area fraction | Sum WG+GB area fraction |
|---|---|---|---|---|---|---|---|---|---|---|---|
| LAE-As extruded | | | 0 | | | | | 0 | | | 0 |
| LAF-As forged | | | 0 | | | | | 0 | | | 0 |
| LFF | | | 0 | | | | | 0 | | | 0 |
| LFW | | | 0 | | | | | 0 | | | 0 |
| LFW760-10 | | | 0 | | | 0.050 | ------- | 10 | 0.00001 | ---------- | 0.00001 |
| LFW760-100 | | | 0 | | | 0.104 | 0.049 | 52 | 0.00015 | 0.00013 | 0.00015 |
| LFW760-1k | | | 0 | | | 0.171 | 0.115 | 157 | 0.00148 | 0.00100 | 0.00148 |
| LFW843-10 | | | 0 | | | 0.077 | 0.038 | 17 | 0.00003 | 0.00002 | 0.00003 |
| LFW843-100 | | | 0 | | | 0.144 | 0.039 | 193 | 0.00095 | 0.00043 | 0.00095 |
| LFW843-1k | | | 0 | | | 0.288 | 0.160 | 173 | 0.00418 | 0.00181 | 0.00418 |
| LFW927-10 | | | 0 | | | 0.146 | 0.050 | 246 | 0.00131 | 0.00063 | 0.00131 |
| LFW927-99 | | | 0 | | | | | 0 | | | 0 |
| LFW927-1k | | | 0 | | | | | 0 | | | 0 |

TABLE 7.—EQUIVALENT RADIUS AND AREA FRACTION OF $M_3B_2$ BORIDES WITHIN GRAINS (WG)
AND AT GRAIN BOUNDARIES (GB), SAMPLE CONDITIONS DESCRIBED IN TABLE 1

| Sample | $M_3B_2$: WG average radius, μm | WG StDev radius, μm | Count, n | WG average area fraction | WG StDev area fraction | GB average radius, μm | GB StDev radius, μm | Count, n | GB average area fraction | GB StDev area fraction | Sum WG+GB area fraction |
|---|---|---|---|---|---|---|---|---|---|---|---|
| LAE-As extruded | 0.200 | 0.084 | 17 | 0.00018 | 0.00015 | 0.262 | 0.113 | 176 | 0.00333 | 0.00029 | 0.00351 |
| LAF-As forged | 0.276 | 0.100 | 18 | 0.00034 | 0.00031 | 0.359 | 0.158 | 7 | 0.00023 | 0.00033 | 0.00057 |
| LFF | | | 0 | | | | | 0 | | | 0.00000 |
| LFW | 0.178 | 0.109 | 2 | 0.00002 | 0.00003 | | | 0 | | | 0.00002 |
| LFW760-10 | | | 0 | | | | | 0 | | | 0.00000 |
| LFW760-100 | 0.364 | 0.122 | 10 | 0.00033 | 0.00026 | | | 0 | | | 0.00033 |
| LFW760-1k | 0.103 | 0.040 | 11 | 0.00003 | 0.00003 | 0.215 | 0.226 | 24 | 0.00051 | 0.00075 | 0.00054 |
| LFW843-10 | | | 0 | | | | | 0 | | | 0.00000 |
| LFW843-100 | | | 0 | | | | | 0 | | | 0.00000 |
| LFW843-1k | 0.402 | 0.118 | 10 | 0.00039 | 0.00036 | 0.285 | 0.049 | 2 | 0.00004 | 0.00008 | 0.00043 |
| LFW927-10 | | | 0 | | | | | 0 | | | 0.00000 |
| LFW927-99 | | | 0 | | | | | 0 | | | 0.00000 |
| LFW927-1k | 0.140 | | 1 | 0.00001 | 0.00001 | 1.186 | 0.618 | 21 | 0.00827 | 0.0055 | 0.00828 |

TABLE 8.—EQUIVALENT RADIUS AND AREA FRACTION OF σ PHASE WITHIN GRAINS (WG)
AND AT GRAIN BOUNDARIES (GB), SAMPLE CONDITIONS DESCRIBED IN TABLE 1

| Sample | σ: WG average radius, μm | WG StDev radius, μm | Count, n | WG average area fraction | WG StDev area fraction | GB average radius, μm | GB StDev radius, μm | Count, n | GB average area fraction | GB StDev area fraction | Sum WG+GB area fraction |
|---|---|---|---|---|---|---|---|---|---|---|---|
| LAE-As extruded | | | 0 | | | | | 0 | | | 0 |
| LAF-As forged | | | 0 | | | | | 0 | | | 0 |
| LFF | | | 0 | | | | | 0 | | | 0 |
| LFW | | | 0 | | | | | 0 | | | 0 |
| LFW760-10 | | | 0 | | | | | 0 | | | 0 |
| LFW760-100 | | | 0 | | | | | 0 | | | 0 |
| LFW760-1k | | | 0 | | | | | 0 | | | 0 |
| LFW843-10 | | | 0 | | | 0.077 | 0.014 | 4 | 0.00001 | 0.00001 | 0.00001 |
| LFW843-100 | 0.163 | 0.081 | 17 | 0.00012 | 0.00009 | 0.216 | 0.166 | 28 | 0.00045 | 0.00033 | 0.00057 |
| LFW843-1k | 0.237 | 0.088 | 129 | 0.00184 | 0.00039 | 0.333 | 0.122 | 51 | 0.00143 | 0.00093 | 0.00327 |
| LFW927-10 | 0.161 | 0.083 | 8 | 0.00006 | 0.00006 | 0.175 | 0.062 | 69 | 0.00053 | 0.00031 | 0.00059 |
| LFW927-99 | | | 0 | | | 0.191 | 0.095 | 24 | 0.00024 | 0.00045 | 0.00024 |
| LFW927-1k | | | 0 | | | | | 0 | | | 0 |

TABLE 9.—OVERALL AREA FRACTIONS OF EACH MINOR PHASE MEASURED IN SAMPLES AGED 1,000 h,
COMPARED TO THOSE PREDICTED AT EQUILIBRIUM USING JMATPRO-NI 6.0 AND PANDAT 8.1

| Temperature, °C | Sample Software | Total MC area fraction | Total $M_{23}C_6$ area fraction | Total $M_3B_2$ area fraction | Total σ area fraction |
|---|---|---|---|---|---|
| 760 | LFW760-1k | 0.00217 | 0.00148 | 0.00054 | 0.00000 |
| 760 | JMatPro | 0.00053 | 0.00546 | 0.00376 | 0.05249 |
| 760 | Pandat | 0.00000 | 0.00648 | 0.00376 | 0.08748 |
| 843 | LFW843-1k | 0.00184 | 0.00418 | 0.00042 | 0.00327 |
| 843 | JMatPro | 0.00206 | 0.00178 | 0.00376 | 0.01208 |
| 843 | Pandat | 0.00000 | 0.00615 | 0.00376 | 0.06263 |
| 927 | LFW927-1k | 0.00300 | 0.00000 | 0.00827 | 0.00000 |
| 927 | JMatPro | 0.00281 | 0.00000 | 0.00375 | 0.00000 |
| 927 | Pandat | 0.00000 | 0.00557 | 0.00375 | 0.03482 |
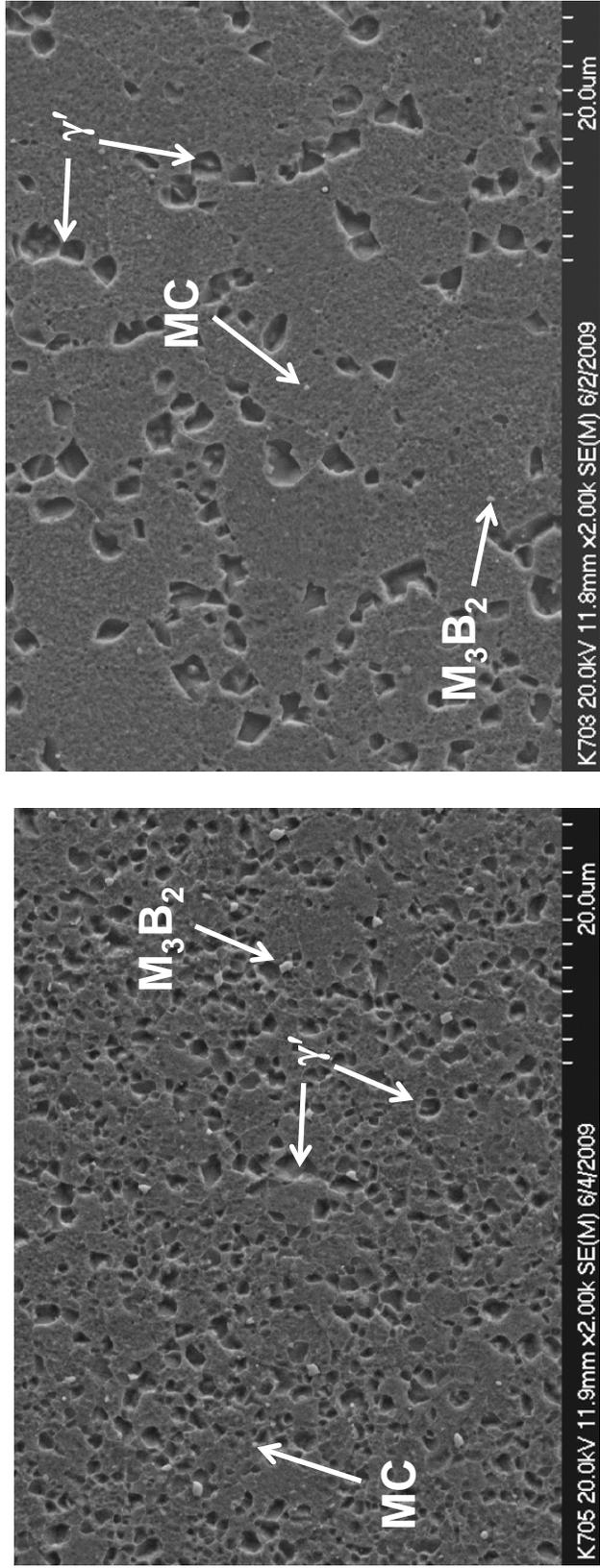
Figure 1.—Comparison of microstructures: a. LAE-as extruded, b. LAF-extruded and isothermally forged.
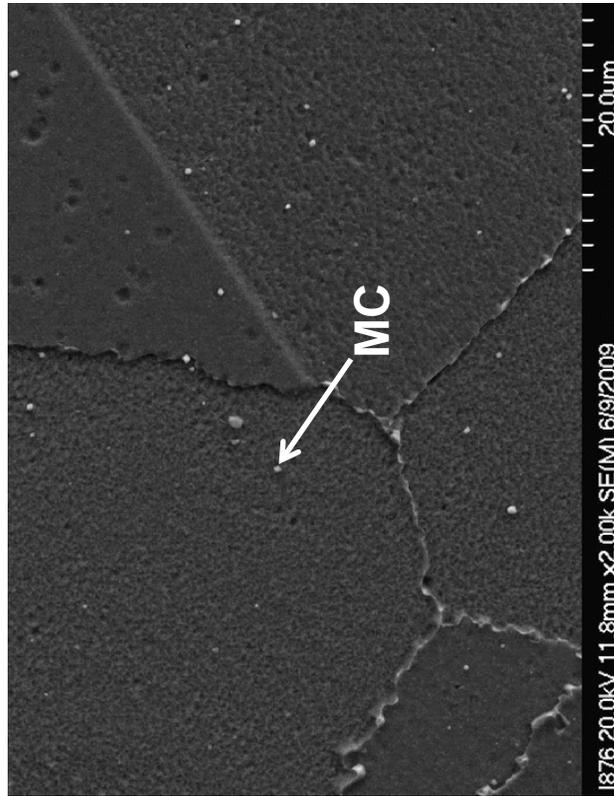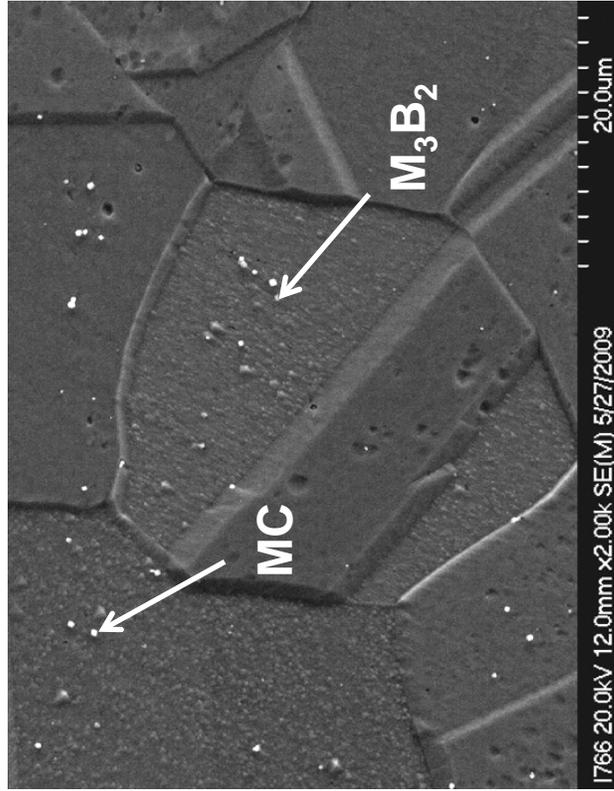
Figure 2.—Comparison of microstructures subsequently heat treated: a. LFF, b. LFW.
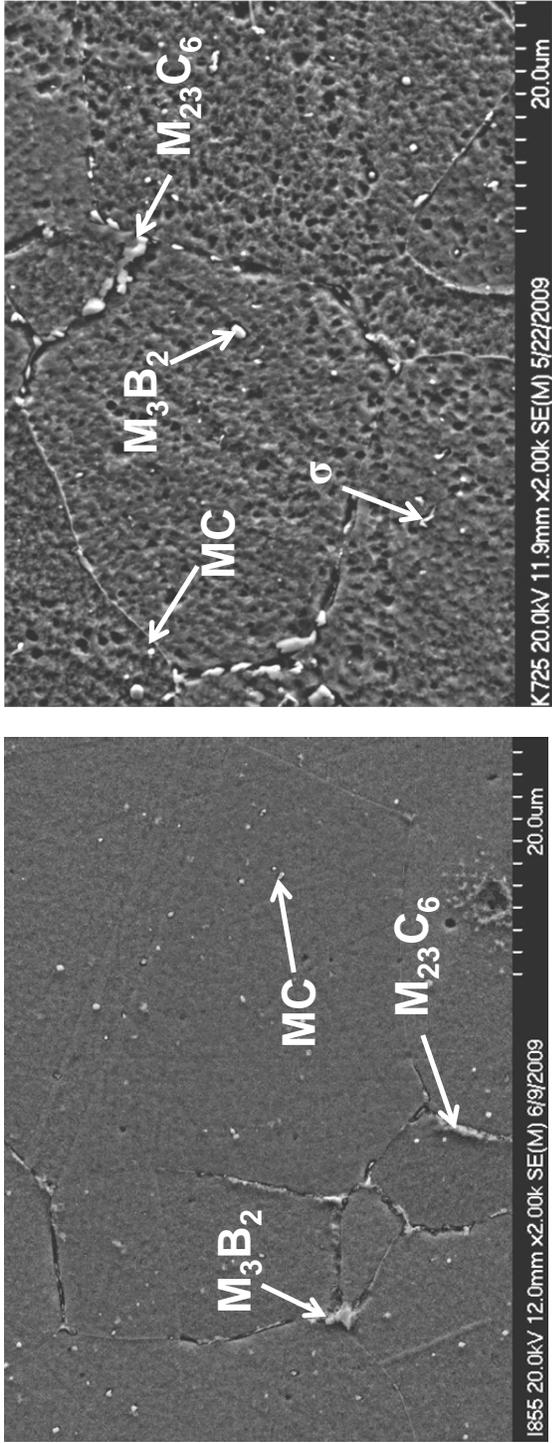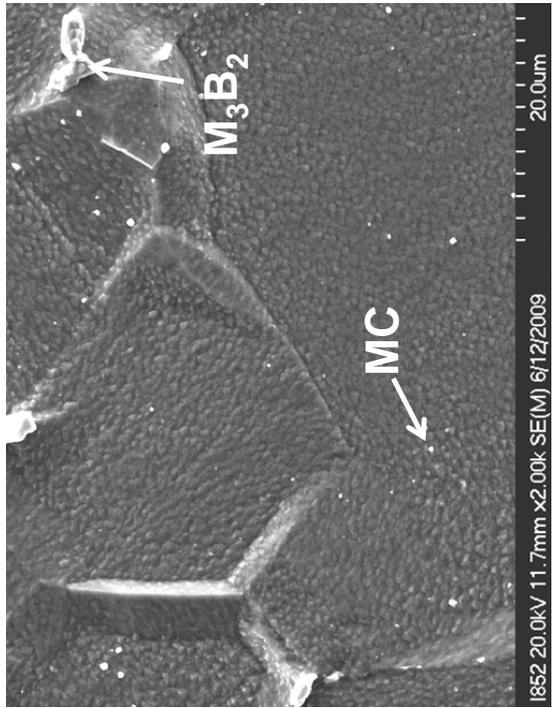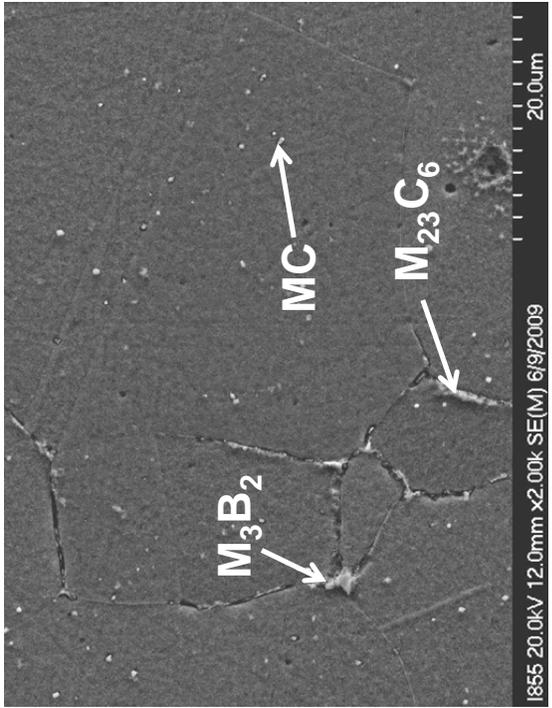
Figure 3.—Images of 1199 °C /1 h/WQ samples additionally aged 1,000 h: a. LFW760-1k, b. LFW843-1k, and c. LFW927-1k.
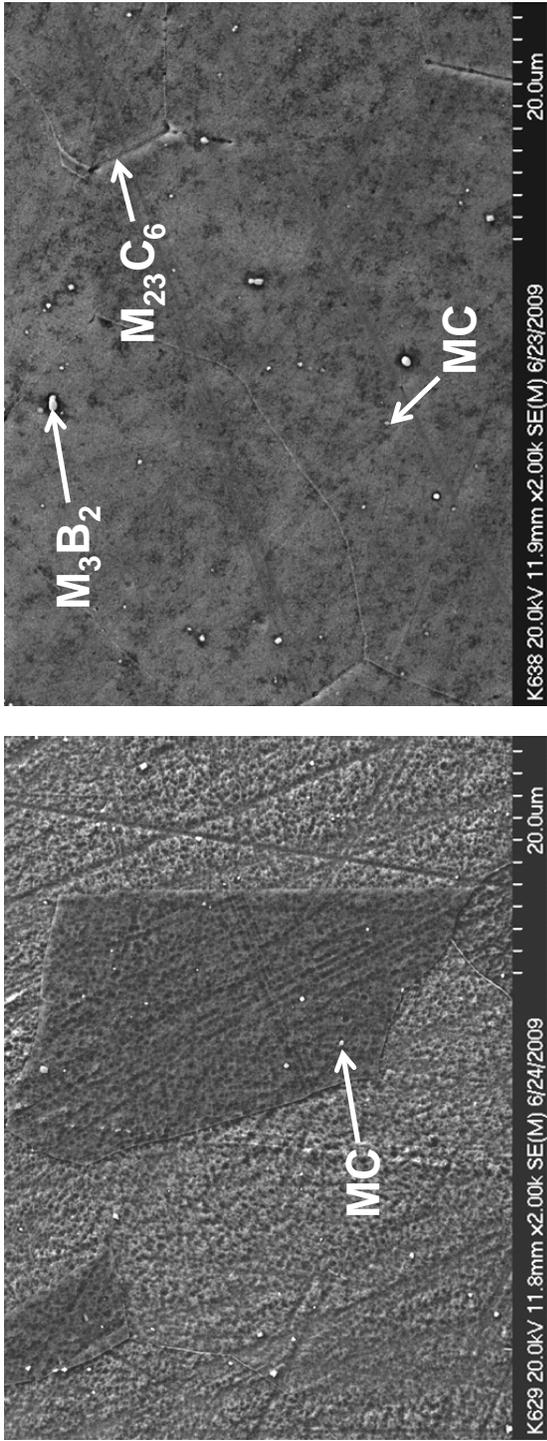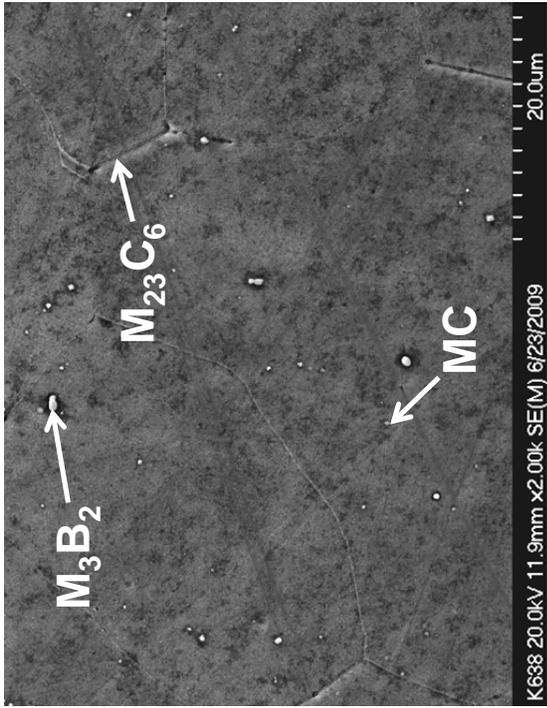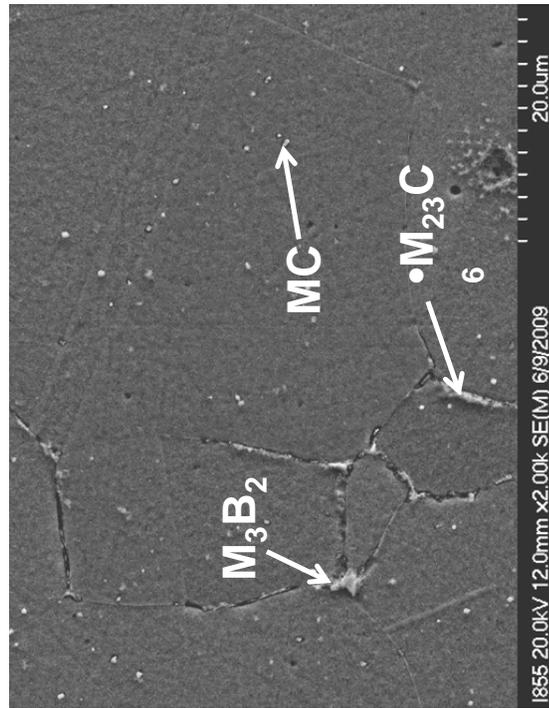
Figure 4.—Images of 1199 °C/1 h/WQ samples additionally aged at 760 °C: a. LFW760-10, b. LFW760-100, and c. LFW760-1,000.
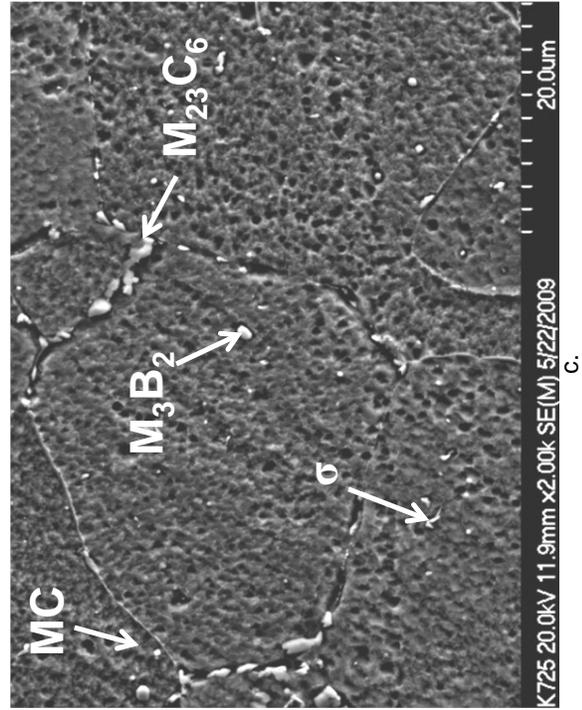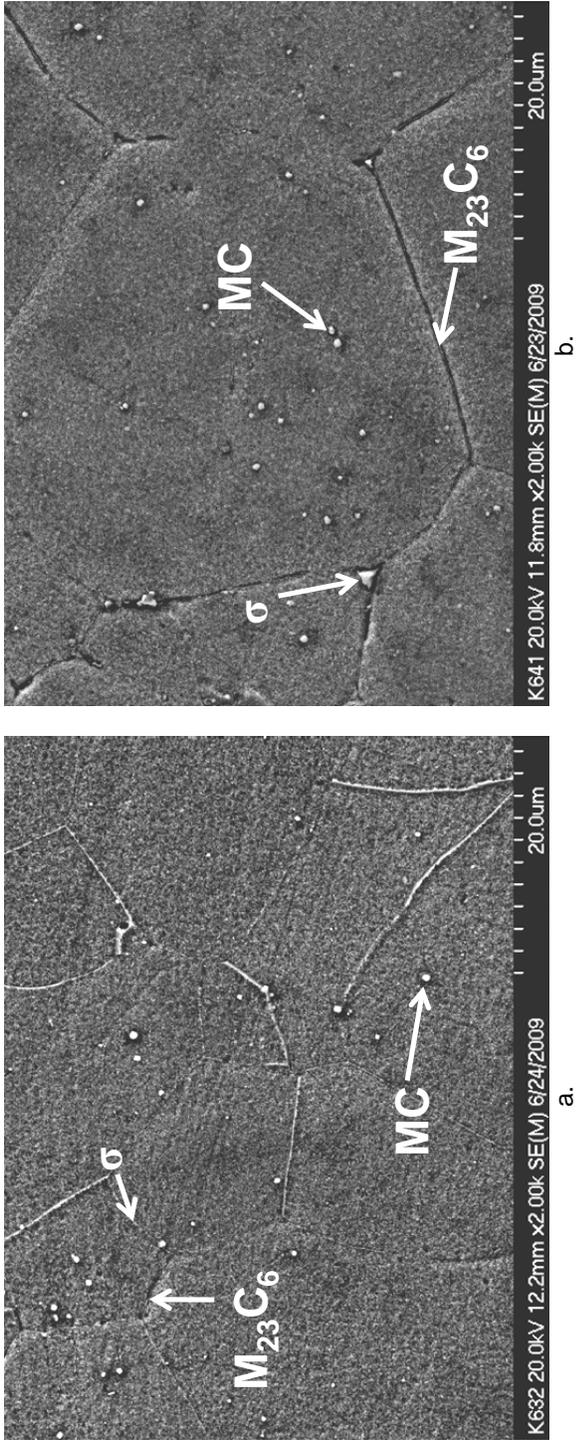
Figure 5.—Images of 1199 °C/1 h/WQ samples additionally aged at 843 °C: a. LFW843-10, b. LFW843-100, and c. LFW843-1k.
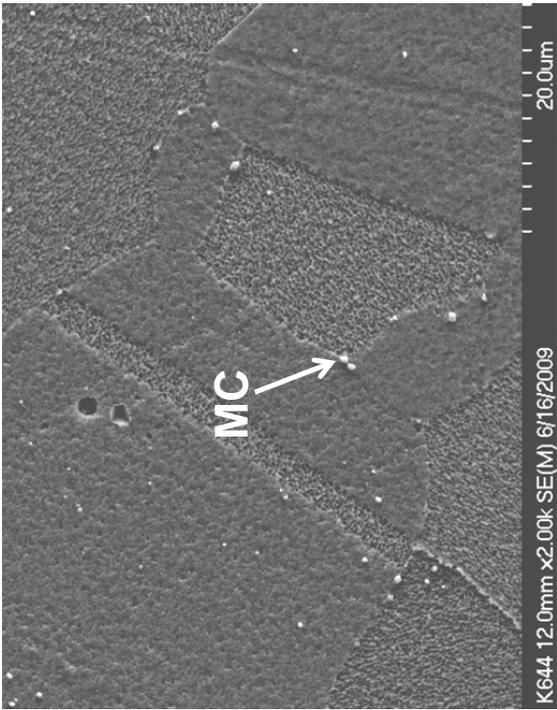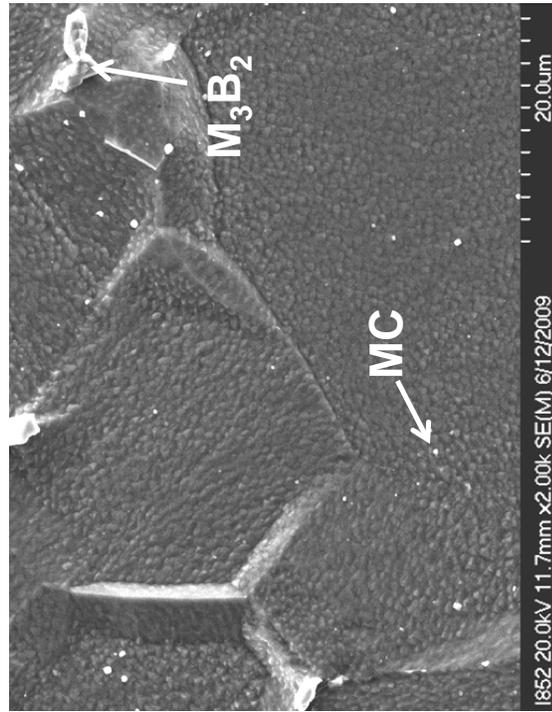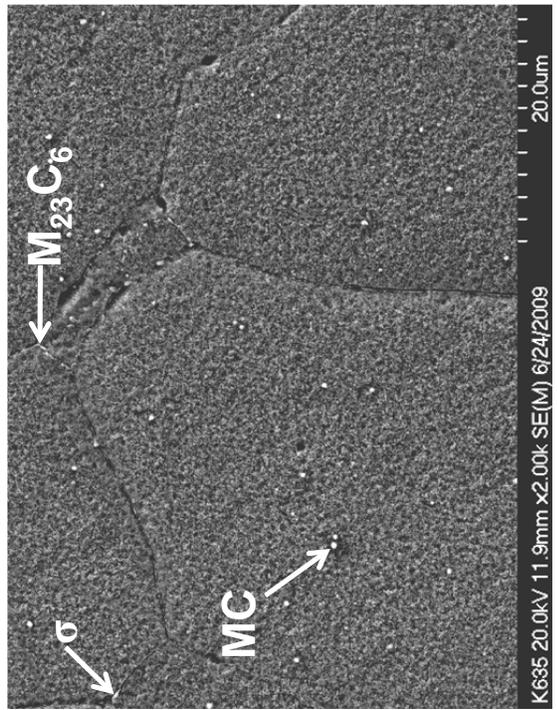
Figure 6.—Images of 1199 °C/1 h/WQ samples additionally aged at 927 °C: a. LFW927-10, b. LFW927-99, c. LFW927-1k.
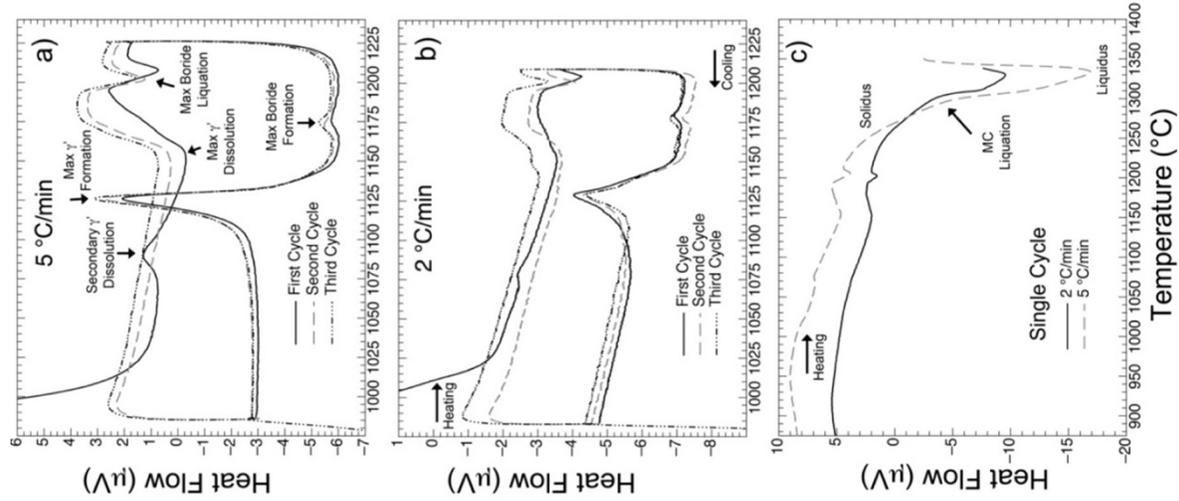
Figure 7.—Thermograms acquired from differential thermal analysis of as-forged LSHR samples that were a) triple cycled at 5 °C/min, b) triple cycled at 2 °C/min and c) single cycled through melting at 5 and 2 °C/min.
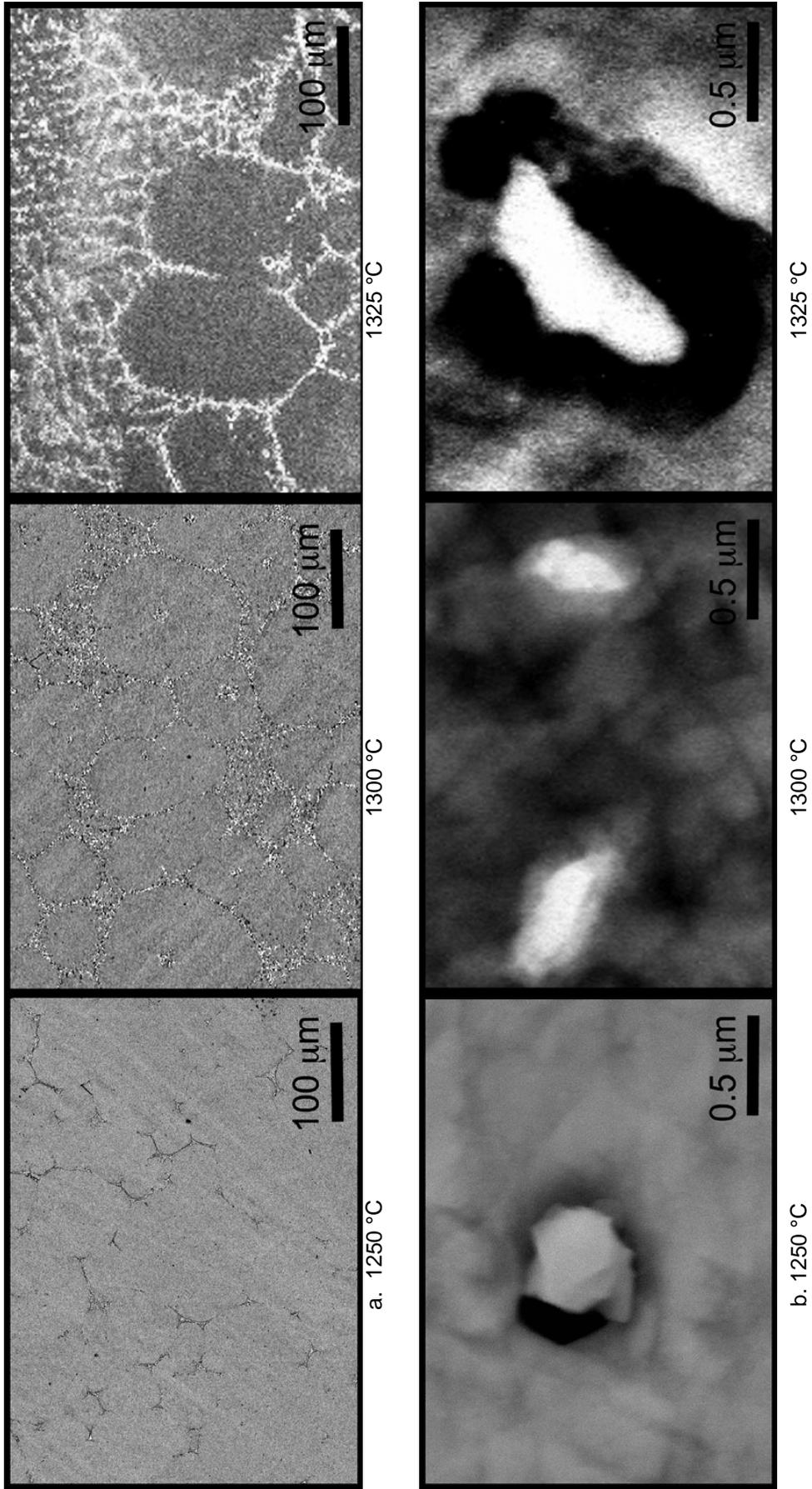
Figure 8.—Heated treated as-forged LSHR samples in air for 1 h at 1250 °C, 1300 °C, 1325 °C and water quenched showing: a. the degree of resolidification and b. MC carbides.
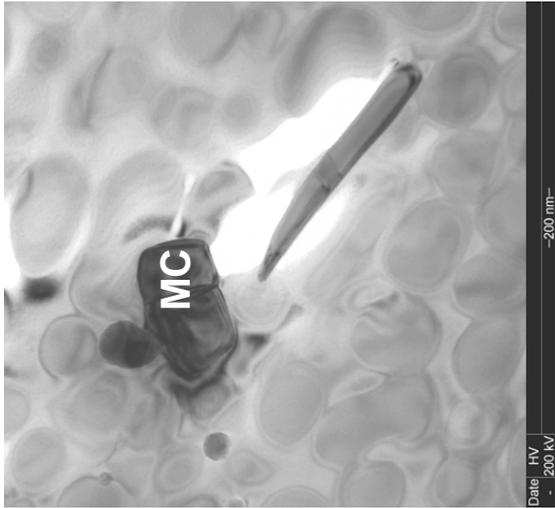
a.
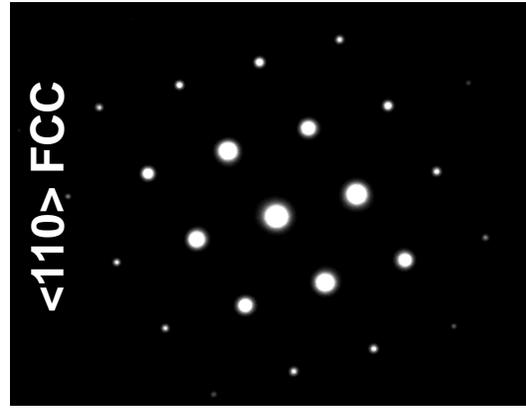


b.

Figure 9.—MC carbide phase, FCC, Fm3m, a~4.3 A: a. TEM image and b. SAEDP of LFW760-1k.
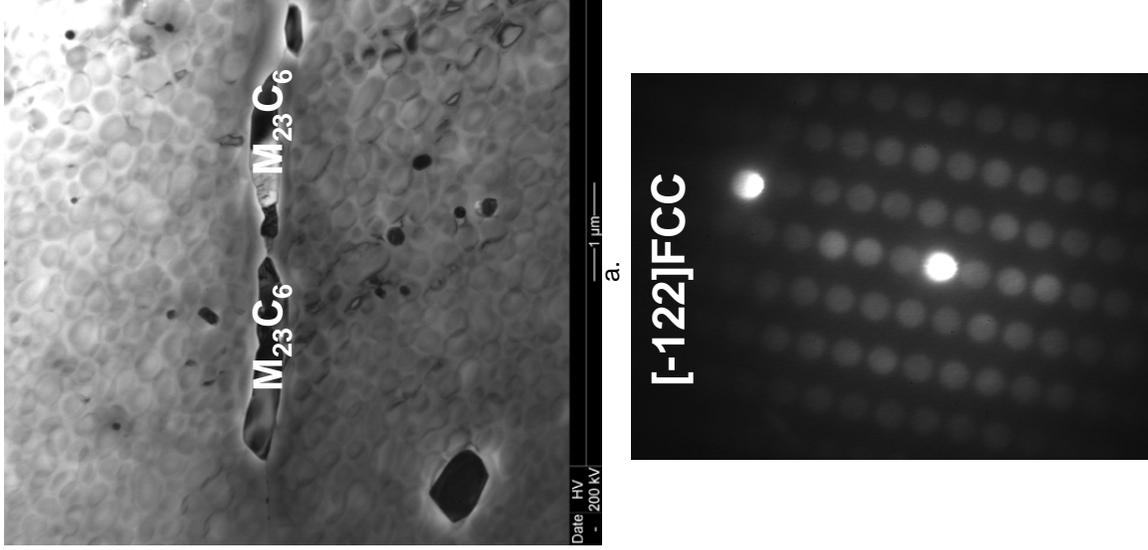
Figure 10.—M$_{23}$C$_6$ carbide, FCC, Fm3m, a ~ 10.6 Å: a. TEM image and b. SAEDP of LFW760-1k.
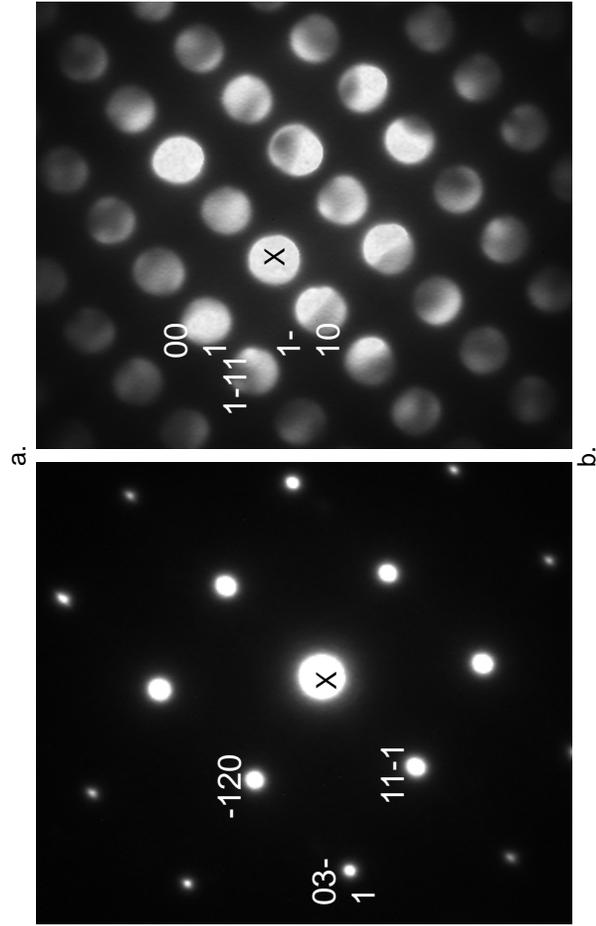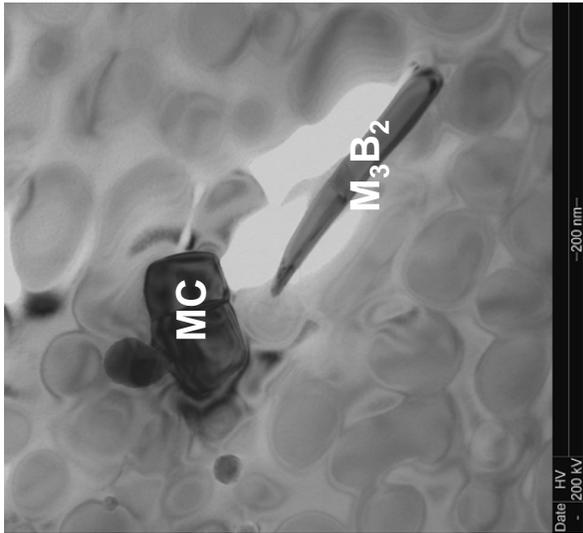
Figure 11.—M$_3$B$_2$ boride phase, tetragonal, P4/mbm, a ~ 6.0 Å, c ~ 3.15 Å: a. TEM image and b. SAEDP of LFW927-1k.
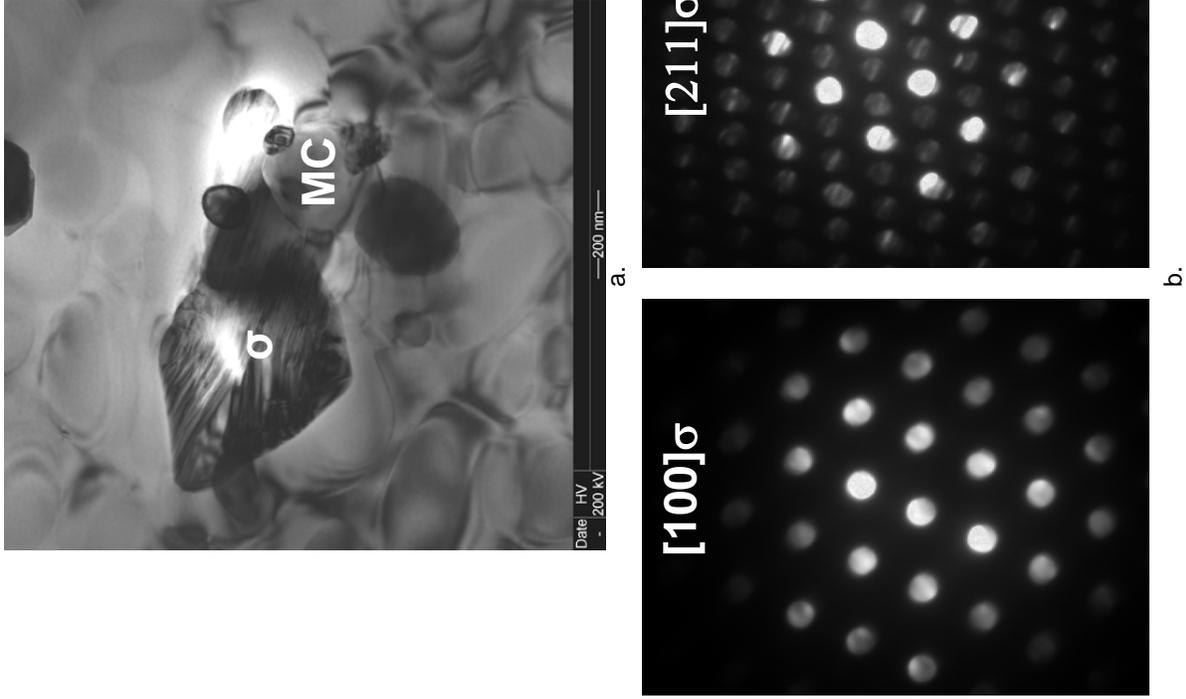
Figure 12.—σ phase, tetragonal, P42/mnm, a ~ 8.9 Å, c ~ 4.6 Å : a. TEM image and b. SAEDP of LFW843-1k.
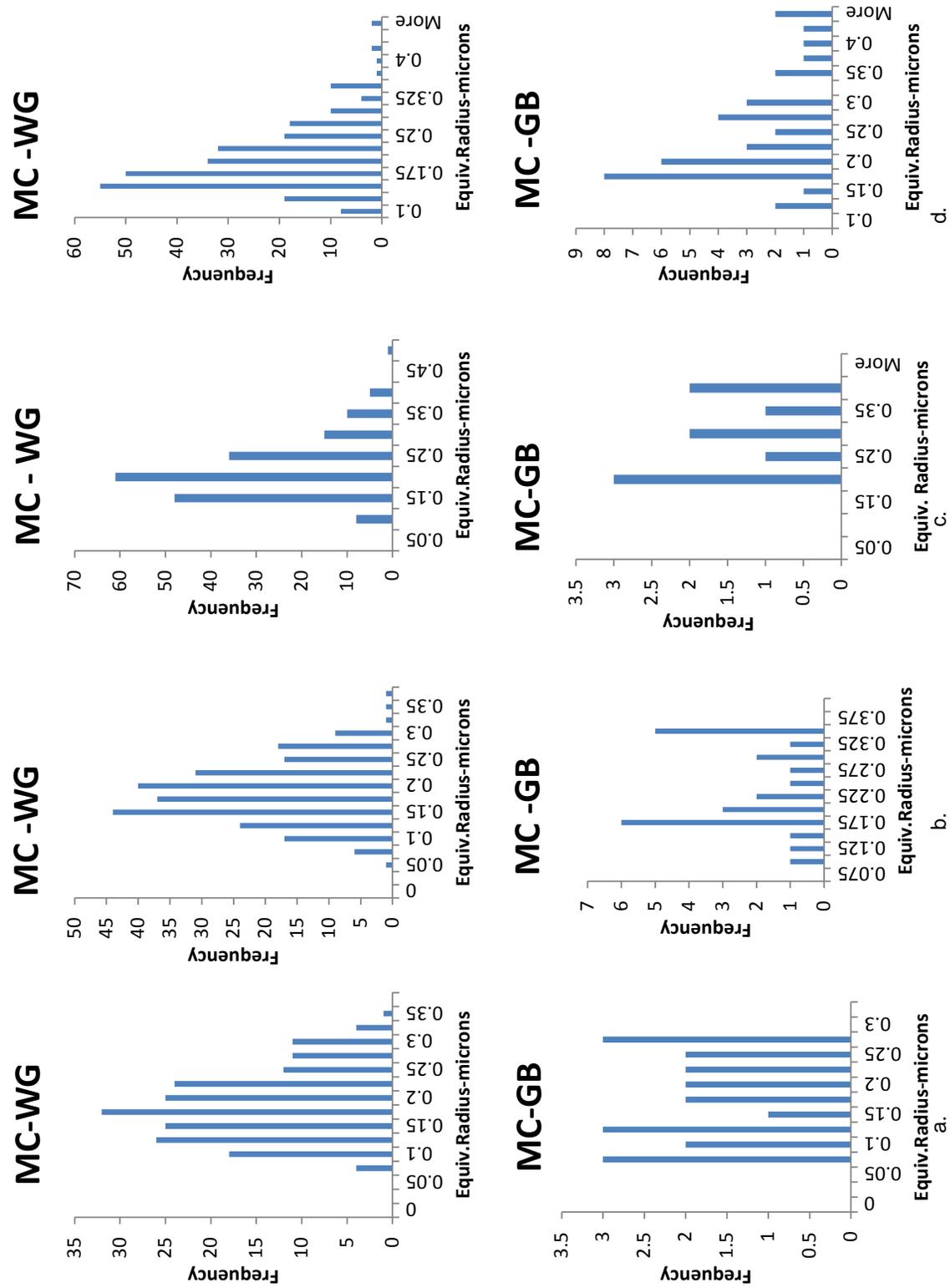
Figure 13.—Typical histograms of equivalent radius vs. frequency for MC carbides within grains (WG) and at grain boundaries (GB): a. LFW, b. LFW760-1k, c. LFW843-1k, d. LFW927-1k.
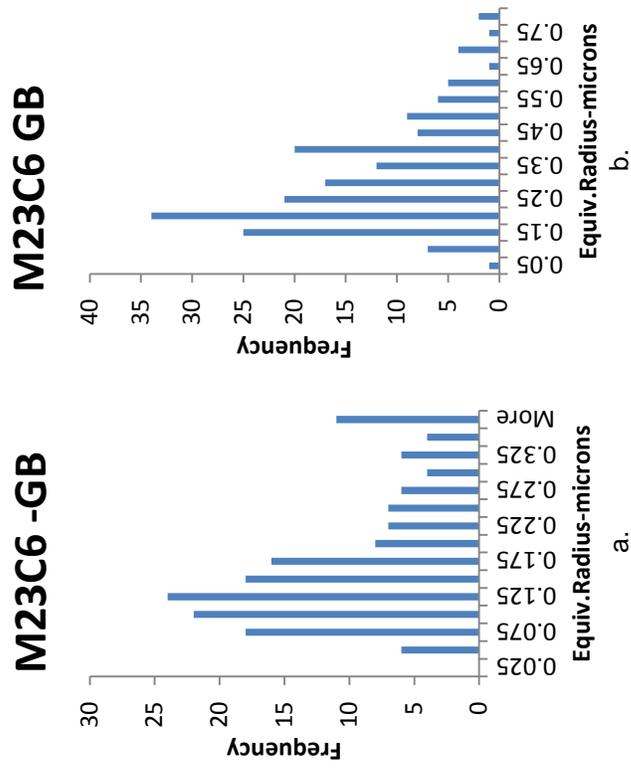
Figure 14.—Typical histograms of equivalent radius vs. frequency for $M_{23}C_6$ carbides, only observed at grain boundaries (GB): a. LFW760-1k, b. LFW843-1k.
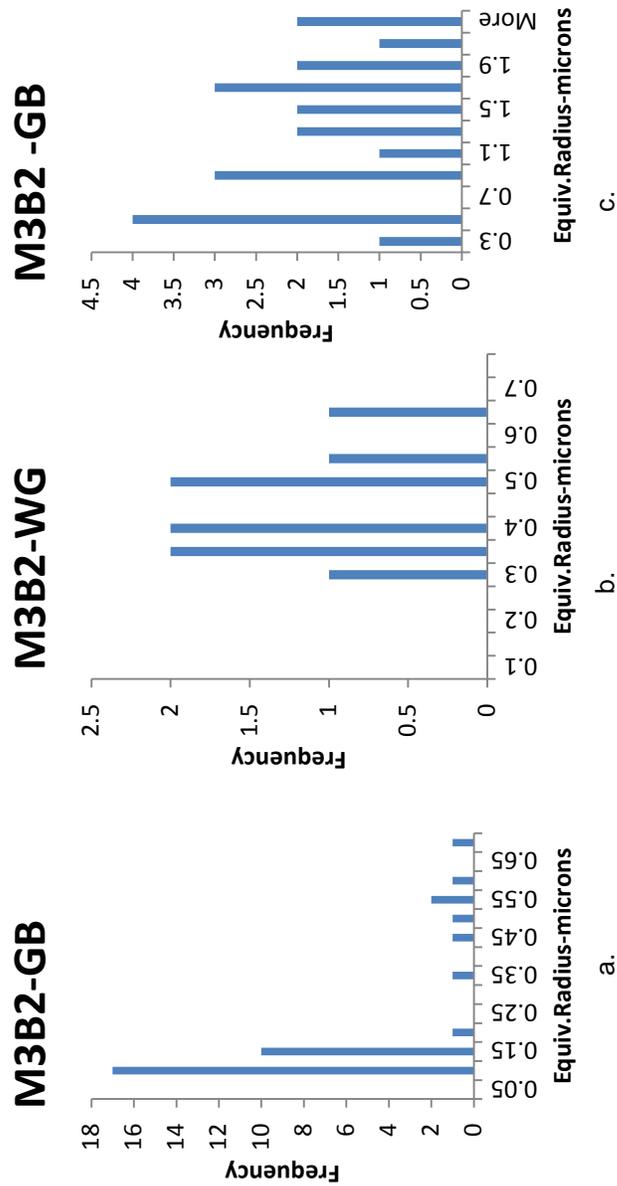
Figure 15.—Typical histograms of equivalent radius vs. frequency for $M_3B_2$ borides within grains (WG) and at grain boundaries (GB): a. LFW760-1k, b. LFW843-1k, c. LFW927-1k.
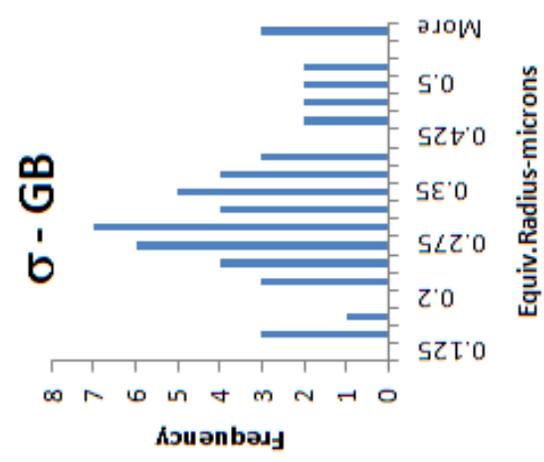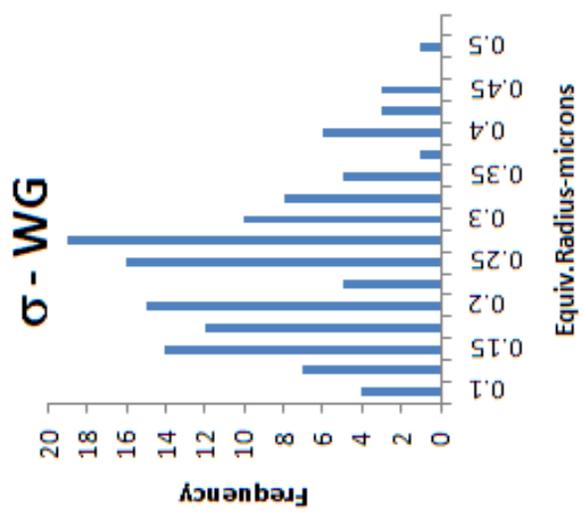
Figure 16.—Histograms of equivalent radius vs. frequency for σ phase in LFW843-1k.
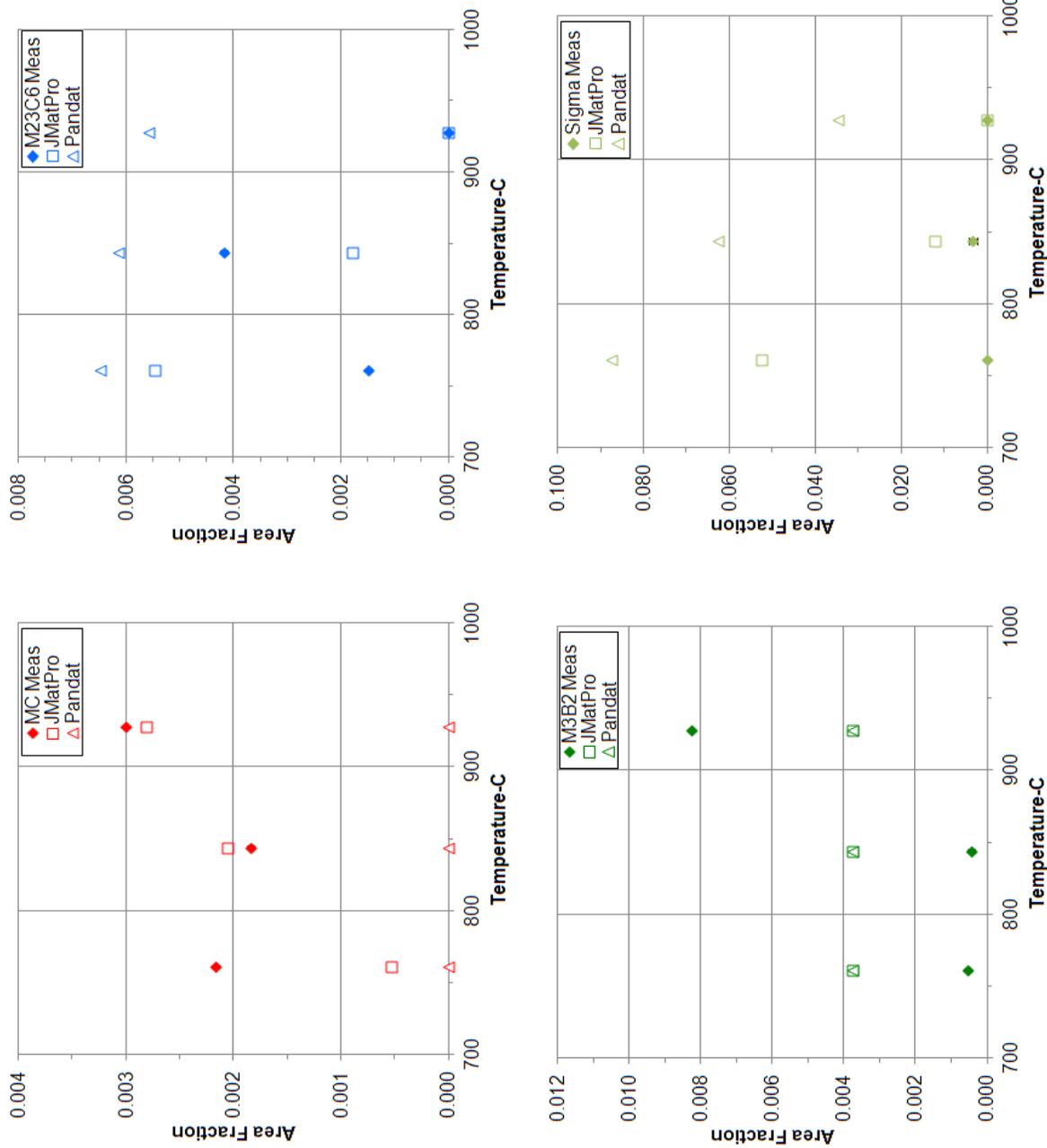
Figure 17.—Overall area fractions of each minor phase measured in samples aged 1,000 h, compared to those predicted at equilibrium using JMatPro-Ni 6.0 and Pandat 8.1.
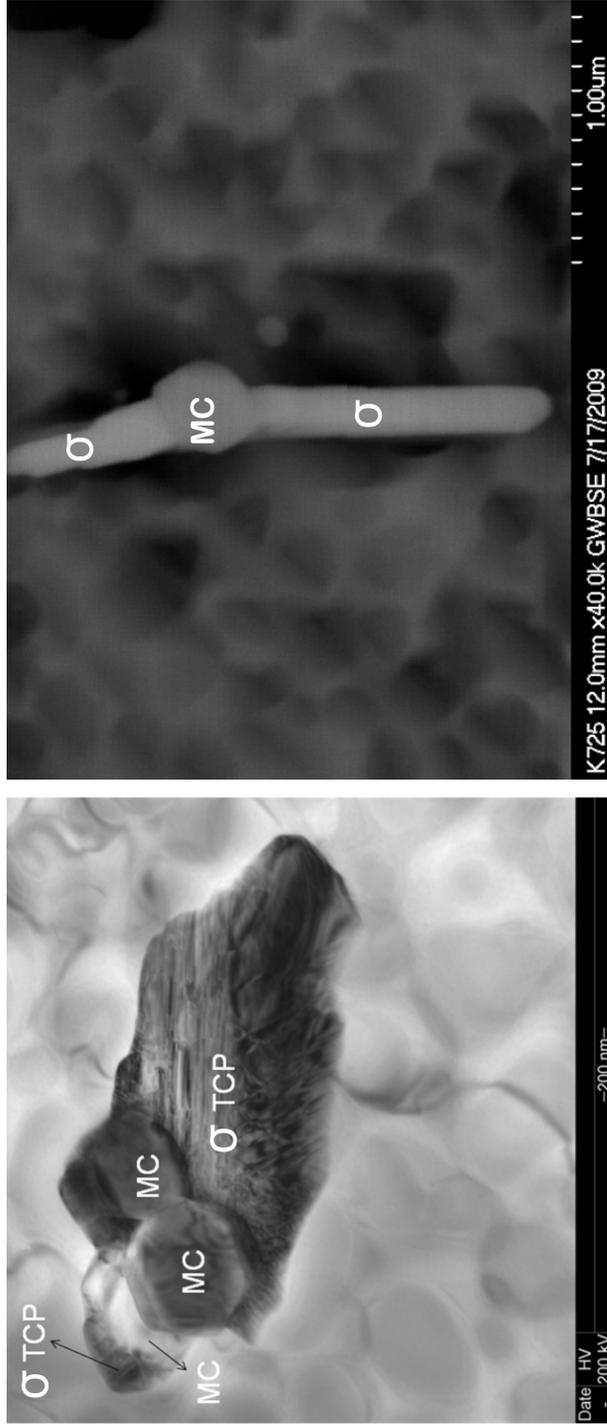
Figure 18.—TEM images from LFW843-1k of σ TCP phase attached to MC carbide, suggesting preferential σ phase nucleation there.

| 1. REPORT DATE *(DD-MM-YYYY)* 07-01-2012 | 2. REPORT TYPE Technical Memorandum | 3. DATES COVERED *(From - To)* |
|---|---|---|
| **4. TITLE AND SUBTITLE** Formation of Minor Phases in a Nickel-Based Disk Superalloy | | **5a. CONTRACT NUMBER** |
| | | **5b. GRANT NUMBER** |
| | | **5c. PROGRAM ELEMENT NUMBER** |
| **6. AUTHOR(S)** Gabb, T., P.; Garg, A.; Miller, D., R.; Sudbrack, C., K.; Hull, D., R.; Johnson, D.; Rogers, R., B.; Gayda, J.; Semiatin, S., L. | | **5d. PROJECT NUMBER** |
| | | **5e. TASK NUMBER** |
| | | **5f. WORK UNIT NUMBER** WBS 561581.02.08.03.15.14 |
| **7. PERFORMING ORGANIZATION NAME(S) AND ADDRESS(ES)** National Aeronautics and Space Administration John H. Glenn Research Center at Lewis Field Cleveland, Ohio 44135-3191 | | **8. PERFORMING ORGANIZATION REPORT NUMBER** E-18185 |
| **9. SPONSORING/MONITORING AGENCY NAME(S) AND ADDRESS(ES)** National Aeronautics and Space Administration Washington, DC 20546-0001 | | **10. SPONSORING/MONITOR'S ACRONYM(S)** NASA |
| | | **11. SPONSORING/MONITORING REPORT NUMBER** NASA/TM-2012-217604 |
| **12. DISTRIBUTION/AVAILABILITY STATEMENT** Unclassified-Unlimited Subject Category: 07 Available electronically at http://www.sti.nasa.gov This publication is available from the NASA Center for AeroSpace Information, 443-757-5802 | | |
| **13. SUPPLEMENTARY NOTES** | | |

**14. ABSTRACT**
The minor phases of powder metallurgy disk superalloy LSHR were studied. Samples were consistently heat treated at three different temperatures for long times to approximate equilibrium. Additional heat treatments were also performed for shorter times, to then assess non-equilibrium conditions. Minor phases including MC carbides, $M_{23}C_6$ carbides, $M_3B_2$ borides, and sigma were identified. Their transformation temperatures, lattice parameters, compositions, average sizes and total area fractions were determined, and compared to estimates of an existing phase prediction software package. Parameters measured at equilibrium sometimes agreed reasonably well with software model estimates, with potential for further improvements. Results for shorter times representing non-equilibrium indicated significant potential for further extension of the software to such conditions, which are more commonly observed during heat treatments and service at high temperatures for disk applications.

**15. SUBJECT TERMS**
Gas turbine engines; Rotating disks

| 16. SECURITY CLASSIFICATION OF: | | | 17. LIMITATION OF ABSTRACT | 18. NUMBER OF PAGES | 19a. NAME OF RESPONSIBLE PERSON STI Help Desk (email:help@sti.nasa.gov) |
|---|---|---|---|---|---|
| **a. REPORT** U | **b. ABSTRACT** U | **c. THIS PAGE** U | UU | 38 | **19b. TELEPHONE NUMBER** *(include area code)* 443-757-5802 |